TECHNIQUES FOR SUB-RESOLUTION SURFACE CHARACTERIZATION
USING COHERENT DIVERSITY MEASUREMENTS

A Thesis

Submitted to the Faculty

of

Purdue University

by

Robert M. Cramblitt

In Partial Fulfillment of the

Requirements for the Degree

of

Doctor of Philosophy

December 1994

REPORT DOCUMENTATION PAGE

Public reporting burden for this collection of information is estimated to average 1 hour per response, including the time for reviewing instructions, searching existing data sources, gathering and maintaining the data needed, and completing and reviewing the collection of information. Send comments regarding this burden estimate or any other aspect of this collection of information, including suggestions for reducing this burden, to Washington Headquarters Services, Directorate for information Operations and Reports, 1215 Jefferson Davis Highway, Suite 1204, Arlington, VA 22202-4302, and to the Office of management and Budget, Paperwork Reduction Project (0704-0188) Washington, DC 20503.

1. AGENCY USE ONLY (Leave Blank)	2. REPORT DATE December 1994	3. REPORT TYPE AND DATES COVERED Final

4. TITLE AND SUBTITLE
Techniques for Sub-Resolution Surface Characterization Using Coherent Diversity Measurements

6. AUTHORS
Robert M. Cramblitt

5. FUNDING NUMBERS

7. PERFORMING ORGANIZATION NAME(S) AND ADDRESS(ES)
Purdue University

AFRL-SR-BL-TR-98-

0014

9. SPONSORING/MONITORING AGENCY NAME(S) AND ADDRESS(ES)
AFOSR/NI
110 Duncan Avenue, Room B-115
Bolling Air Force Base, DC 20332-8080

10. SPONSORING/MONITORING AGENCY REPORT NUMBER

11. SUPPLEMENTARY NOTES

12a. DISTRIBUTION AVAILABILITY STATEMENT
Approved for Public Release

12b. DISTRIBUTION CODE

13. ABSTRACT *(Maximum 200 words)*
See attached.

DTIC QUALITY INSPECTED 2

14. SUBJECT TERMS	15. NUMBER OF PAGES
	16. PRICE CODE

17. SECURITY CLASSIFICATION OF REPORT Unclassified	18. SECURITY CLASSIFICATION OF THIS PAGE Unclassified	19. SECURITY CLASSIFICATION OF ABSTRACT Unclassified	20. LIMITATION OF ABSTRACT UL

ACKNOWLEDGMENTS

TABLE OF CONTENTS

LIST OF TABLES

LIST OF FIGURES

ABSTRACT

Cramblitt, Robert M. Ph.D., Purdue University, December, 1994. Techniques for Sub-resolution Surface Characterization Using Coherent Diversity Measurements. Major Professor: Dr. Mark R. Bell.

This dissertation examines the feasibility of obtaining small-scale surface information from frequency-diverse measurements of surfaces that are stochastically described by a regularity model. This parametric point-process model describes a one-dimensional surface in terms of the mean and variance of the inter-scatterer distances, and can represent scatterer distributions ranging from totally random to nearly periodic. The problem of estimating model parameters from measured spectra is solved by optimizing the total squared-error between closed-form approximations of the mean power spectra of finite-length data intervals and the simple periodogram. The dissertation examines the general performance limitations of such a procedure, determining how approximation error, signal-to-noise ratio and frequency-sampling rate affect the feasibility and accuracy of parameter estimation. We find that parameter estimation is feasible at frequency-sampling rates that are well below that suggested by the PSD. This suggests that it is possible to obtain parameter estimates by comparing sparse narrow-band frequency measurements to the PSD of the point-process, thereby obtaining information about the surface on sub-resolution scales.

The dissertation extends the model to describe marked point processes. We discover that ignoring the marks can cause significant estimation error when estimating the regularity model parameters in the presence of mark noise. Joint estimation of the regularity and mark parameters is feasible only when the variance of the marks is large with respect to their mean. Accounting for the marks can, however, allow the regularity parameters to be accurately estimated in the presence of mark noise.

1. INTRODUCTION

Accurate classification and characterization of image regions is often an important goal for the users of coherent imaging systems, such as synthetic aperture radar (SAR) and B-scan ultrasound. Image classification can be thought of as an inverse scattering problem, in which information about scattering surfaces must be inferred from coherently detected images of the surface. Some classes of surfaces may be described by parametric stochastic models, in which case knowledge of the model parameters, rather than of the scatterers themselves, is sufficient to describe the surface. Surfaces in which elemental scatterers are arranged with some degree of periodicity are one such class. The energy backscattered from coherently illuminating these surfaces exhibits interference effects which can be exploited to obtain stochastic descriptions of the surfaces and to extend the scale on which a system makes useful measurements. We demonstrate this principle with an example which provides the motivation to adopt a particular kind of point scatterer model. After describing the model and reviewing its second order statistics, we develop an approximation for the mean power spectrum of measured signals which is utilized in an optimized estimation scheme to extract model parameters from frequency-diverse measurements.

To illustrate the effect that surface structure can have on a coherent system, consider this simple case: a broadband pulse, $p(t)$, is transmitted and scattered by a very long, one-dimensional collection of equi-spaced, unit-reflectivity scatterers. The received signal is $r(t) = p(t) \star s(t)$, where $\star$ denotes convolution and

$$s(t) = \sum_i \delta(t - iT) \tag{1.1}$$

is called the scatterer function. The scatterer spacing, T, is expressed as a temporal delay time ($T = 2d/v$, where d is a spatial distance and v is the velocity of propagation in the medium). $p(t)$ may also represent a system impulse or point spread function,

so we will simply refer to it as the system response. The spectrum of the received signal is

$$R(f) = LP(f)S(f) = LP(f)\frac{1}{T}\sum_i \delta(f - \frac{i}{T}), \qquad (1.2)$$

where P and S are the Fourier transforms of p and s, respectively, and $L < 1$ represents an effective loss parameter. It consists of impulses separated by the inverse of the scatterer spacing, so the spectrum is highly structured. The case in which scatterers are randomly spaced represents the opposite extreme. In this case, the scatterer function for a finite interval of scatterers becomes a sum of unit-magnitude random-phase phasors, and the power spectrum is a constant, independent of frequency, so it exhibits no structure at all. Intermediate cases generate a power spectrum that displays a combination of these behaviors.

Parametric regularity models have been proposed to describe the distribution of scatterers in such a way that the parameters of the model will allow both regular and random scatterer spacing, as well as the more interesting intermediate cases. The model takes the form of a renewal point process, one which is very well described in the literature. Regularity models arose out of applications of pulse frequency modulation control methods to neural system modelling [1], and were applied to acoustic scattering problems by Landini and Verrazzani [2]. They gave examples of biological tissue structures exhibiting various degrees of regularity and demonstrated the feasibility of using this feature to distinguish between classes of tissues using ultrasound measurements. Their measurements were of tissues with periodic structures on scales larger than the system resolution, so the bandwidth was wide enough to capture the spectral peaks suggested by the regularity model. The simple Poisson point processes that had been used to model acoustic scattering phenomena prior to Landini and Verrazzani's paper would correspond only to the case of completely random scatterer spacings. Wear, et al., applied autoregressive (AR) modelling techniques to the problem of estimating the mean inter-scatterer spacing of regularly spaced scatterers embedded in a volume of randomly spaced ones [3]. AR methods provide resolution capabilities superior to non-parametric methods when lengths of the measurement

intervals are close to the mean scatterer spacing. Their methods do not incorporate a parametric model which accounts for the stochastic nature of the inter-scatterer spacings.

The ability to characterize a scattering surface by estimating model parameters from frequency-diverse measurements depends on the frequency-measuring capabilities of the system. For some systems, the spectral peaks may fall completely within the system bandwidth, so that information on the scatterer spacing is incorporated into the measured data. In other systems, the peaks may be farther apart than the bandwidth, but may be detected by exploiting frequency-agile features of the system. If the system has sufficient agility, its composite bandwidth may be wide enough to encompass the peaks. The possibility exists, however, that the frequency domain structure can be discerned from only a few measurements at a sparse set of frequencies. In this event, the information about scatterer spacing is measured even though the scatterer spacing is smaller than the system resolution.

Neither regularity models nor point processes in general have been applied to radar scatterer modelling. Many radar systems have been constructed with frequency-agile abilities [4], and therefore have the potential to exploit the properties of the regularity model to characterize sub-resolution structure. The model may not prove useful for SAR image analysis problems because the system bandwidths are too narrow to measure the spectral structure imparted by the regularity of surface scatterers [5]. The advent of multi-frequency SAR systems [6], however, suggests that the frequency-sampling capabilities needed to exploit this structure may soon be at hand.

Applications of radar systems for remote measurement and characterization abound in the fields of agriculture, oceanography and geophysics [7]. SAR imagery, for example, has found an application in the problem of ground cover classification [8]. In such an application, regularity models could potentially be used to distinguish periodic structures, such as crop rows, from random structures such as forest canopy or meadows, in cases where the wavelengths were not short with respect to the row separation. Some analyses have explicitly attempted to include effects caused by the

regular nature of crops. Ulaby et al., for example, developed a backscatter model which characterizes the regular undulations of a bare tilled field with random perturbations [9], but this is not a point process model. To the extent that forests could be modelled as a collection of water-filled tree-trunks, regularity measurements could be used to characterize the density of trees and the variance of their spacing, which may conceivably be related to physical parameters such as the age and species of the trees. Ocean wave measurements are a frequent application of both SAR and other radar systems. Ocean waves would be expected to exhibit various degrees of regularity depending on the local wind velocity and sea state, both of which are often measured using wave data. The sensitivity of radars to small scale capillary and gravity waves in the form of Bragg resonance is well known [10], so regularity models may prove quite useful in characterizing ocean patches on small scales. Currie, et al., described the measurement of snow fields by wideband radars, noting that the characteristic scatterer spacing was well below the resolving capability of the measurement system (0.5 m) , despite its wide bandwidth (640 MHz centered at 35 GHz) [4]. This may be a case in which such small-scale information about the distribution of scattering centers might be obtained from a sparse set of narrowband measurements taken over a frequency range of many gigaHertz.

Regularity models can also be used to describe incoherently measured signals, such as passive measurements of the sounds generated by knee joints. Zhang, et al. [11], applied very similar models to describe these signals, although their assumption of Gaussian interarrival statistics violates some basic assumptions of the derivation, and they simulate ordinary, rather than stationary, renewal processes (this difference is discussed in Chapter 2). Nonetheless, this application demonstrates that regularity models can be used to characterize phenomenon which are more general than those encountered in coherent measurement scenarios. In fact, they can be applied to any signal which can be represented as the convolution of an impulse response with a stationary point process.

Another passive measurement application is the analysis of electro-myography (EMG) signals produced by measuring action potentials with electrodes in human muscle. In certain cases, the regularity model parameters may provide a quantitative means of describing this data. We are currently investigating this possibility.

In the next chapter, we examine the regularity model in detail and discuss its power spectrum. The following chapter presents a developement of some closed-form expressions that approximate the mean power spectra of finite-length measurements of surfaces decribed by the model. We evaluate the accuracy of these expressions in Chapter 4. Chapter 5 describes how these expressions can be used in an optimization method to estimate the model parameters, and we assess the feasibility of this approach. Finally, in Chapters 6 to 8 we extend these results to models that allow the scatterers to have non-unit reflectivity.

2. SURFACE REGULARITY MODELS

The surface regularity model treats the scatterers as points of a renewal point process in which the distances between points are gamma-distributed. This model is described by only two parameters, but by varying them it can describe a great range of scatterer spatial regularity behavior. Specifically, the model can produce cases in which the scatterers are very regularly spaced (hence the name "surface regularity") as well as cases in which the spacing is entirely random.

We will assume that the surface illuminated and viewed by the coherent system is a one-dimensional collection of uniformly reflective scatterers. The system transmits a pulse, and the observed temporal response of the system to the surface is

$$r(t) = p(t) \star s(t), \tag{2.1}$$

where $p(t)$ represents the impulse response of the entire system. We assume that $p(t)$ is known. Since it completely incorporates the effects of scatterers on the received signal, we will call

$$s(t) = \sum_i \delta(t - T_i) \tag{2.2}$$

the scatterer function, in which the $\{T_i\}$ are an ordered sequence of scatterer locations expressed as temporal delay times. $s(t)$ is the stochastic function whose attributes we wish to determine. We will assume that the scatterers are the points of a stationary renewal process (or infinite impulse process). The $\{T_i\}$, defined so that $T_0 \leq 0 \leq T_1$, are then the recurrence times from the origin of the renewal process. We define $\{\tau_i = T_i - T_{i-1}\}$ to be the inter-arrival times of the process, which are to be distinguished from the inter-scatterer (or inter-event) times $\{x_i\}$. The inter-arrival times

are differences between recurrence times which are measured with respect to an arbitrary *time origin*, while the inter-scatter times are differences between event times which are measured with respect to an arbitrary *event* [12].

In the regularity model, we assume that the inter-scatterer times $\{x_i\}$ are independent, identically distributed (i.i.d.) random variables from a gamma(α,β) distribution, whose density function is given by

$$f(x) = \frac{x^{\alpha-1}e^{-x/\beta}}{\Gamma(\alpha)\beta^\alpha} \quad \alpha, \beta, x > 0, \tag{2.3}$$

where $\Gamma(\alpha)$ is the gamma function,

$$\Gamma(\alpha) = \int_0^\infty t^{\alpha-1}e^{-t}dt. \tag{2.4}$$

The mean and variance of the inter-scatterer times are $\bar{x} = \alpha\beta$ and $\sigma_x^2 = \alpha\beta^2 = \bar{x}^2/\alpha$, respectively. Thus, for a given mean inter-scatterer spacing, $\bar{x}$, the variance of the inter-scatterer times is controlled by varying the model order, α. If α is large, the variance of the inter-scatterer times becomes small, and the scatterers become very regularly spaced. In the limiting case, the scatterers have a periodic spacing. If $\alpha = 1$, the $\{x_i\}$ are exponentially distributed and the model reduces to a Poisson point process (also called white Poisson noise). In this case, the scatterers appear to have a random placement and the degree of regularity is considered small. Values of α less than unity cause the scatterers to appear clustered.

For any stationary renewal process, the inter-arrival time about the origin must have a density function given by

$$f_{\tau_1}(\tau) = \frac{\tau f(\tau)}{\bar{x}} \tag{2.5}$$

and all other inter-arrival times must have the same density as the $\{x_i\}$. When the inter-scatterer times have a gamma(α, β) distribution, τ_1 will have a gamma($\alpha+1, \beta$) distribution. The first recurrence time, T_1 must have the distribution

$$f_{T_1}(t) = \frac{1 - F(t)}{\bar{x}}, \tag{2.6}$$

where $F(t)$ is the distribution function for the inter-scatterer times.

We now wish to determine the power spectrum of the measurements, $r(t)$, when the scatterer spacings are described statistically by the regularity model. The power spectral density (PSD) of the received signal is

$$\Phi_r(\omega) = |P(\omega)|^2 \Phi_s(\omega), \tag{2.7}$$

where $P(\omega)$ is the known frequency response of the system (the Fourier transform of $p(t)$) and $\Phi_s(\omega)$ is the PSD of the random process $s(t)$. First, consider the stationary renewal process, $s(t)$. Both Cox and Lewis [12] and Leneman [13] derived general expressions for the autocorrelation and PSD of such a process, with the former given by

$$\phi_s(t) = \begin{cases} \dfrac{1}{\alpha\beta}\left[\delta(t) + \displaystyle\sum_{n=1}^{\infty} f_n(t)\right] & t \geq 0 \\ \Gamma_s(-t) & t < 0 \end{cases} \tag{2.8}$$

where f_n is the density function of the sum of n independent inter-scatterer times,

$$f_n(t) = \begin{cases} f(t) \star f_{n-1}(t), & n > 1 \\ f(t) & n = 1. \end{cases} \tag{2.9}$$

The summation in (2.8) is called the renewal density.

The PSD is the Fourier transform of (2.8):

$$\Phi_s(\omega) = \frac{1}{\alpha\beta}\left[1 + \sum_{n=1}^{\infty}\left(F(\omega)^n + F(-\omega)^n\right)\right], \tag{2.10}$$

where $F(\omega)$ is the Fourier transform of $f(t)$, which, for the gamma density, is

$$F(\omega) = \int_{-\infty}^{\infty} f(x)e^{-\jmath\omega x}dx = (1 + \jmath\omega\beta)^{-\alpha}. \tag{2.11}$$

In this case, F is the complex conjugate of the characteristic function of f.

Since

$$|F(\omega)|^2 = (1 + \omega^2\beta^2)^{-\alpha} < 1, \tag{2.12}$$

when $\omega \neq 0$ the geometric series in (2.10) may be evaluated and terms rearranged to find that

$$\Phi_s(\omega) = \frac{1}{\bar{x}}\left[\frac{|Z|^2 - 1}{|Z - 1|^2}\right], \tag{2.13}$$

where $Z = 1/F(\omega)$. Although straightforward in its derivation, this rather compact form of the PSD has not appeared in the body of work dealing with regularity models. It is valid for all valid values of α, unlike the forms presented by Sanderson [1] and Gestri and Piram [14], which are only valid for integer values of α. These forms do, however, explicitly show the presence of a delta function at the origin, which is hidden in (2.13). Landini and Verrazzani used Sanderson's PSD formula in their acoustic scattering work.

Sanderson derived the autocorrelation of the scatterer function by expressing the Laplace transform of the renewal density in terms of its poles, and inverting to get

$$
\phi_s(t) = \begin{cases} \dfrac{1}{\alpha\beta}\left[\delta(t) + \dfrac{1}{\alpha\beta} + \dfrac{2}{\alpha\beta}\displaystyle\sum_{k=2}^{(\alpha+1)/2} e^{-\alpha_k t}\cos(\omega_k t + \theta_k)\right] & \alpha \text{ odd}, \ t \geq 0, \\[3mm] \dfrac{1}{\alpha\beta}\left[\delta(t) + \dfrac{1}{\alpha\beta}(1 - e^{-2t/\beta}) + \dfrac{2}{\alpha\beta}\displaystyle\sum_{k=2}^{\alpha/2} e^{-\alpha_k t}\cos(\omega_k t + \theta_k)\right] & \alpha \text{ even}, \ t \geq 0, \\[3mm] \phi_s(-t) & t < 0 \end{cases}
$$

(2.14)

where

$$
\theta_k \;=\; \frac{2\pi(k-1)}{\alpha}, \tag{2.15}
$$

$$
\alpha_k \;=\; \frac{1}{\beta}(1 - \cos\theta_k), \tag{2.16}
$$

$$
\omega_k \;=\; \frac{1}{\beta}\sin\theta_k. \tag{2.17}
$$

The PSD of the process is given by

$$
\Phi_s(\omega) = \begin{cases} \dfrac{1}{\alpha\beta}\left[1 + \dfrac{2\pi}{\alpha\beta}\delta(\omega) + \dfrac{2}{\alpha\beta}\displaystyle\sum_{k=2}^{(\alpha+1)/2} S_k(\omega,\omega_k)\right] & \alpha \text{ odd} \\[3mm] \dfrac{1}{\alpha\beta}\left[1 + \dfrac{2\pi}{\alpha\beta}\delta(\omega) - \dfrac{1}{\alpha\beta}S_{(\alpha+2)/2}(\omega) + \dfrac{2}{\alpha\beta}\displaystyle\sum_{k=2}^{\alpha/2} S_k(\omega,\omega_k)\right] & \alpha \text{ even} \end{cases}
$$

(2.18)

where

$$
S_k(\omega,\omega_k) \;=\; \frac{\alpha_k\cos\theta_k + (\omega - \omega_k)\sin\theta_k}{\alpha_k^2 + (\omega - \omega_k)^2} + \frac{\alpha_k\cos\theta_k - (\omega + \omega_k)\sin\theta_k}{\alpha_k^2 + (\omega + \omega_k)^2}, \tag{2.19}
$$

$$
S_{(\alpha+2)/2}(\omega) \;=\; 2\left[\frac{2/\beta}{(2/\beta)^2 + \omega^2}\right]. \tag{2.20}
$$

Note that Sanderson had an errant factor of two multiplying $S_{(\alpha+2)/2}$ in (2.18). Sanderson points out that expressing the PSD in this fashion shows that it is the sum of terms which have peaks at the frequencies $\{\omega_k\}$, although it should be noted that the maxima of the PSD do not occur at these locations. Sanderson's formula also allows us to evaluate the PSD at the origin, disregarding the delta function, which we will do shortly.

Gestri and Piram [14] derived an alternate expression for the PSD, but did not use Sanderson's Laplace transform method, leading to an expression in complex form given by

$$\Phi_s(\omega) = \begin{cases} \dfrac{1}{\alpha\beta}\left[1 + \dfrac{2\pi}{\alpha\beta}\delta(\omega) + \dfrac{2}{\beta^2}\displaystyle\sum_{r=2}^{\alpha} \dfrac{\epsilon_r(\epsilon_r - 1)}{[\omega^2 + (\epsilon_r - 1)^2/\beta^2]\displaystyle\prod_{\substack{k=0 \\ k \neq r}}^{\alpha}(\epsilon_r - \epsilon_k)}\right] & \alpha \geq 2 \\ \dfrac{1}{\alpha\beta}\left[1 + \dfrac{2\pi}{\alpha\beta}\delta(\omega)\right] & \alpha = 1, \end{cases}$$

(2.21)

where

$$\epsilon_0 = 0, \tag{2.22}$$

$$\epsilon_r = e^{j2\pi r/\alpha}. \tag{2.23}$$

This formulation may appear simpler than Sanderson's, but the actual implementation is computationally problematic because of the limitations imposed by most software packages on the precision of complex number representations.

Figures 2.1 and 2.2 illustrates the spectral structure that develops as the model order, α, increases from 10 to 100. In the Poisson process case, $\alpha = 1$, the PSD is equal to $1/\bar{x}$ everywhere except at the origin. In all of the figures presented in this thesis, the average inter-scatterer spacing, $\bar{x}$, is set to unity, and the frequency axis is in units of Hertz, so peaks in the spectrum occur near integer frequencies. The spacing between peaks is controlled by $\bar{x}$, while the dominance and number of peaks is determined by α. As the maxima grow with increasing α, their locations approach
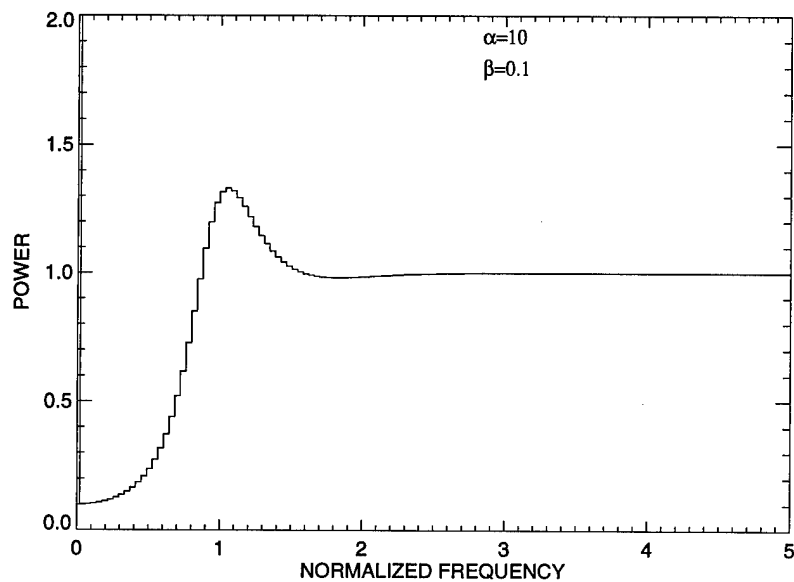
Figure 2.1 PSD of the scatterer function for the regularity model for a low value of model order.
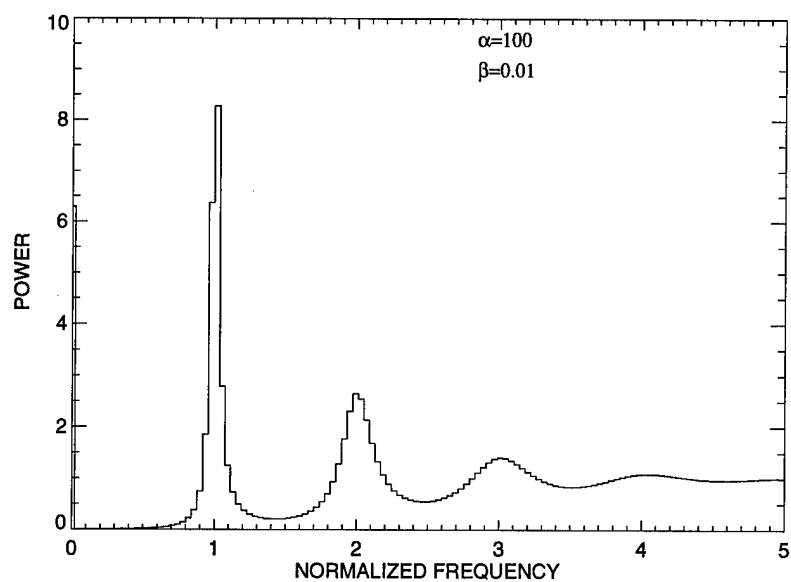
Figure 2.2 PSD of the scatterer function for the regularity model with a very regular scatterer distribution.

multiples of $1/\bar{x}$ from the right, although their displacement from these frequencies is always small. Estimates of $\bar{x}$ derived solely from the locations of the maxima, therefore, may be biased.

Examination of Sanderson's formula shows that the PSD at the origin consists of the sum of a constant and a delta function: $2\pi\delta(\omega)/\bar{x}^2 + 1/(\alpha\bar{x})$, $\alpha \geq 1$. At high frequencies, the variance of the inter-scatterer distances becomes large with respect to a wavelength and the spectral structure disappears, with the PSD becoming a constant value of $1/\bar{x}$. As α becomes larger, the spectral structure extends to higher frequencies.

Real data are always truncated to finite-length sample intervals, either by some form of range gating or by data editing. Truncation is equivalent to multiplication of the received signal with a window function $w_T(t)$, which has support on an interval of length T:

$$w_T(t) = \text{rect}(t/T) \equiv \begin{cases} 1 & t \in [-T/2, T/2] \\ 0 & \text{else.} \end{cases} \tag{2.24}$$

The truncated signal can be written

$$r_w(t) = w_T(t - T_0)(p(t) \star s(t)), \tag{2.25}$$

where T_0 is an offset representing the location of the sample interval. The mean power spectrum of r_w is then

$$\frac{1}{T}E\left\{|R_w(\omega)|^2\right\} = \left(|P(\omega)|^2\Phi_s(\omega)\right) \star \frac{1}{T}W_T^2(\omega), \tag{2.26}$$

where E denotes expectation and R_w and W_T are the Fourier transforms of r_w and w_T, respectively. The mean spectrum (2.26) converges to the PSD (2.7) as $T \to \infty$.

Ultimately we will estimate the regularity model parameters by comparing measured spectra to theoretical expressions. Two approaches are possible: one can attempt to accurately measure the PSD of the point process and compare this to (2.13), or one can measure the mean power spectrum of finite data intervals and compare this to (2.26). The former approach is more suitable when utilizing sparse, narrow-band measurements. Since we assume that we are given finite data intervals to work with,

we will explore the latter approach. In the next chapter, we will make some assumptions and develop an expression which approximates the mean power spectrum (2.26) of an interval of the infinite impulse process. Since the window is incorporated into the expression, use of the approximation eliminates the need to perform a convolution on the PSD to compare it with measured power spectra, which can offer computational advantages, especially when accuracy is desired. Although non-parametric spectral estimates based on rectangular window functions have limitations [15], a closed-form expression can be quite useful when it is the model parameters, rather than the PSD, that are of interest. Like (2.13), our approximation will have the added benefit of being free of the limitation that α must be an integer.

3. POWER SPECTRUM APPROXIMATIONS

This section considers simplifications to the PSD expressions presented above. We begin by noting that the system frequency response, $P(\omega)$, is often fairly smooth over its passband. It is also reasonable to expect to analyze data intervals that are longer than the impulse response (or point spread function, for imaging systems) so that the window function has a narrower bandwidth than the system. These assumptions are true, for example, for the sample acoustic system analyzed by Landini and Verrazzani, as well as the for the range response of the SEASAT SAR system described by Fitch [5]. Munson's analysis of SAR processing shows this to be a general property of strip-mapping SAR systems [16]. Under these conditions, the system response can be taken outside of the convolution in (2.26),

$$E\{|R_w(\omega)|^2/T\} \approx |P(\omega)|^2(W_T(\omega)^2 \star \Phi_s(\omega)/T), \qquad (3.1)$$

which is the equivalent of moving the window function inside the convolution in (2.25):

$$r_w(t) \approx \tilde{r}_w(t) \equiv p(t) \star w_T(t - T_0)s(t). \qquad (3.2)$$

This approximation is equivalent to ignoring the fact that, given an interval of length T, some signal in the interval is due to the convolution of $p(t)$ with points just outside the interval, and that the convolution of points near the interior ends of the interval with $p(t)$ will give rise to a non-zero signal outside of the interval. We will assume that the known $P(\omega)$ has a conveniently wide bandwidth, and that we can compensate for any significant in-band variations. We can then concentrate on the rightmost terms in (3.2), and ignore the specific forms required for $p(t)$ when a particular system is considered. If a system is specified, the appropriate power spectra may be weighted accordingly.

The rightmost terms in (3.2) represent the scatterer function truncated to a T-length interval, and can be re-expressed as

$$s_T(t) = w_T(t - T/2)s(t) = \sum_{i=1}^{N_T} \delta(t - T_i), \tag{3.3}$$

where N_t is the counting process corresponding to the point process $s(t)$, i.e., N_t is the number of scatterers falling in the interval $(0, t]$, and, without loss of generality, the origin is chosen so that the window is centered at $T/2$. We shall refer to (3.3) as the truncated scatterer function (TSF). The TSF can also be expressed solely in terms of the point process:

$$s_T(t) = \sum_{i=1}^{\infty} \delta(t - T_i)1_{[0,T]}(T_i) \tag{3.4}$$

where $1_{[\cdot]}(x)$ is the indicator function. The Fourier transform of $s_T(t)$ is

$$S_T(\omega; \alpha, \bar{x}) = \sum_{i=1}^{N_T} e^{-\jmath\omega T_i}, \tag{3.5}$$

where the dependence on the model parameters is made explicit. The mean power spectra of the response function (3.2) is

$$\frac{1}{T}E\left\{\left|\tilde{R}_w(\omega)\right|^2\right\} = |P(\omega)|^2\, \Phi_s^T(\omega; \alpha, \bar{x}), \tag{3.6}$$

where Φ_S^T is the mean TSF power spectrum

$$\Phi_s^T(\omega; \alpha, \bar{x}) = \frac{1}{T}E\left\{|S_T(\omega; \alpha, \bar{x})|^2\right\} = \frac{1}{T}\Phi_s(\omega) \star W_T^2(\omega). \tag{3.7}$$

The convolutional form of (3.7) may be evaluated numerically. Theoretically, the expectation integral may also be evaluated numerically, but in practice the computational burden and difficulty of choosing integration rules for high-order iterated integrals make this option impractical. No exact closed-form expressions appear possible for either form. In order to produce an approximate closed-form expression, note that the mean number of scatterers in the sample interval is $\overline{N_T} = T/\bar{x}$. In addition, the asymptotic distribution of N_T is Gaussian with variance $T\sigma_x^2/\bar{x}^3 = T\bar{x}/\alpha^2$ [17], so the coefficient of variation of N_T, $\sigma_{N_T}^2/\overline{N_T}^2$, approaches zero for large T. For $\bar{x}$ fixed,

increasing α accelerates the convergence to the asymptotic distribution. This suggests that, for large α or T, N_T can be approximated by its mean; consequently (3.3) can be approximated by including in the summation only the contributions from the first $\lceil T/\bar{x} \rfloor$ points of the process, where $\lceil \cdot \rfloor$ denotes rounding to the nearest integer. The scatterer function for the first K process points is

$$s_K(t) = w_{T_K}(t - T_K/2)s(t) = \sum_{i=1}^{K} \delta(t - T_i), \tag{3.8}$$

and its mean power spectrum is given by

$$\Phi_s^K(\omega; \alpha, \bar{x}, T) = \frac{1}{T}E\left\{|S_K(\omega)|^2\right\} = \frac{1}{T}\sum_{m=1}^{K}\sum_{n=1}^{K}E\left\{e^{\jmath\omega(T_m - T_n)}\right\}. \tag{3.9}$$

We shall call (3.8) the approximate truncated scatterer function (ATSF).

The terms of (3.9) in the double sum can be grouped into sets for which $m = n$, $m > n$ and $m < n$. The terms for which $m = n$ sum to K. For the other cases, note that

$$T_m - T_n = \begin{cases} \tau_m + \tau_{m-1} + \cdots + \tau_{n+1} & m > n, \\ -(\tau_n + \tau_{n+1} + \cdots + \tau_{m+1}) & m < n. \end{cases} \tag{3.10}$$

This, plus the fact that the $\{\tau_i : i \geq 2\}$ are i.i.d., means that the expectation can be written in terms of the characteristic function of the $\{x_i\}$, $F^*(\omega)$,

$$E\left\{e^{\jmath\omega(T_m - T_n)}\right\} = \begin{cases} F^*(\omega)^{m-n} & m > n, \\ F^*(-\omega)^{n-m} & m < n. \end{cases} \tag{3.11}$$

Since the $\{x_i\}$ have a gamma distribution, the characteristic function is given by

$$F^*(\omega) = E\left\{e^{\jmath\omega x}\right\} = (1 - \jmath\omega\beta)^{-\alpha} \equiv Z^{-1}. \tag{3.12}$$

The expectation can now be expressed as

$$E\left\{|S_K(\omega)|^2\right\} = K + \sum_{m=1}^{K}\left(\sum_{n=m+1}^{K}F^*(-\omega)^{n-m} + \sum_{n=1}^{m-1}F^*(\omega)^{m-n}\right) \tag{3.13}$$

and by using

$$\sum_{m=1}^{K}\sum_{n=m+1}^{K}g(n-m) = \sum_{m=1}^{K}\sum_{n=1}^{m-1}g(m-n) \tag{3.14}$$

it becomes

$$E\left\{|S_K(\omega)|^2\right\} = K + \sum_{m=1}^{K}\sum_{n=1}^{m-1}\left(F^*(\omega)^{m-n} + F^*(-\omega)^{m-n}\right). \qquad (3.15)$$

By grouping terms for which $m - n$ is constant, the double sum (3.14) can be further simplified:

$$\sum_{m=1}^{K}\sum_{n=1}^{m-1} g(m-n) = \sum_{n=1}^{K} ng(K-n), \qquad (3.16)$$

so the expectation becomes

$$E\left\{|S_K(\omega)|^2\right\} = K + \sum_{n=1}^{K-1} n\left[F^*(\omega)^{K-n} + F^*(-\omega)^{K-n}\right]. \qquad (3.17)$$

These sums are variations of the finite sums of geometric progressions, and we can use

$$\sum_{n=1}^{K-1} nZ^{-(K-n)} = \frac{Z^{-(K-1)} + (K-1)Z - K}{(1-Z)^2} \equiv G(Z). \qquad (3.18)$$

and the fact that $F^*(-\omega) = F(\omega)$, to finally write the mean power spectrum of the ATSF as

$$\Phi_s^K(\omega; \alpha, \bar{x}, T) = \frac{1}{T}\left[K + 2\Re\left\{G(Z)\right\}\right], \qquad (3.19)$$

where $\Re\{\cdot\}$ denotes the real part. This derivation is only valid, and only makes sense, when K is an integer. We note, however, that (3.19) varies continuously with K, and that the transition between integer cases is a smooth one, for $\lceil T/\bar{x}\rceil \leq K \leq \lceil T/\bar{x}\rceil + 1$. Allowing K to become real-valued therefore provides a means of interpolating between integer cases. Furthermore, the non-integer cases are empirically in agreement with numerical evaluations of (3.7). In a later chapter, we will use (3.19) in an error minimization procedure in which it is preferable for the error to be a continuous function of α, $\bar{x}$ and T, For these reasons, we define Φ_s^K to be a function of the real-valued $K = T/\bar{x}$.

As in (2.13), α is not limited to the integers. Since the finite length of the sample interval was incorporated into the ATSF, the mean power spectrum of the ATSF also includes finite sample length effects, and we have an approximate analytical expression for the PSD of measured data which obviates the need to convolve a window function with a theoretical PSD, as in (3.7).

At $\omega = 0$, the mean ATSF power spectrum is $K^2/T = (T/\bar{x})^2/T = \overline{N_T}^2/T$. The mean TSF spectrum is $\overline{N_T^2}/T$ at the origin, and the difference between these terms is equal to the variance of N_T. The relative difference between these terms is $(1 + T\alpha^2/\bar{x}^3)$, which approaches zero for large T or α or small $\bar{x}$. It is reasonably small, for fixed $\bar{x}$, unless T and α are close to unity. At large frequencies, the variance of the inter-scatterer distances becomes large with respect to the wavelength, and the power spectrum becomes $K/T = 1/\bar{x}$, as it is for the TSF spectrum and the PSD of the infinite impulse process.

The windowed version of the zero-mean point process (the zero-mean truncated scatterer function (ZTSF)),

$$\bar{s}_T(t) = w_T(t - T/2)(s(t) - 1/\bar{x}), \tag{3.20}$$

can be approximated by

$$\bar{s}_K(t) = w_{T_K}(t - T_K/2)(s(t) - 1/\bar{x}), \tag{3.21}$$

which we call the approximate zero-mean truncated scatterer function (AZTSF). Utilizing the fact that the characteristic function of T_1 is

$$E\{e^{j\omega T_1}\} = \frac{j}{\omega \bar{x}}(1 - Z^{-1}), \tag{3.22}$$

the mean power spectrum of the AZTSF is found to be

$$\Phi_{\bar{s}}^K(\omega; \alpha, \bar{x}, T) = \frac{1}{T}E\left\{|\bar{S}_K(\omega)|^2\right\} = \Phi_s^K(\omega) +$$

$$\frac{1}{T}\left[\frac{2}{(\omega\bar{x})^2}\left(\frac{1}{\omega\bar{x}}\Im\left\{\frac{Z-1}{Z^K}\right\} + \Re\left\{Z^{-K}\right\}\right) - \frac{2}{(\omega\bar{x})}\Im\left\{\frac{Z(1-Z^{-K})}{Z-1}\right\}\right], \tag{3.23}$$

where $\Im\{\cdot\}$ denotes the imaginary part. The value of the mean AZTSF power spectrum at the origin is

$$\Phi_{\bar{s}}^K(0) = \frac{1}{T\bar{x}^2}E\left\{(T - T_K)^2\right\} = \frac{1}{\alpha\bar{x}} - \frac{2}{\alpha T} + \frac{(\alpha+1)(\alpha+2)}{3\alpha^2 T} \tag{3.24}$$

which is proportional to the mean squared difference between T and T_K. Since $\Phi_{\bar{s}}^K(0) = \Phi_{\bar{s}}(0) + O(1/T)$, where $O(x)$, the Bachman-Landau notation, represents a term proportional to x, the AZTSF converges to the PSD at the origin, as does the TSF spectrum.

4. APPROXIMATION ACCURACY

Since closed-form expressions for (3.7) do not exist, none exist for the error between (3.7) and its approximations, which limits the mathematical rigor of an error analysis. The accuracy of the ATSF and AZTSF mean power spectrum formulas may be examined by comparing them to numerical evaluations of the convolution in (3.7) for various values of α and $T/\bar{x}$. The integrated squared-error (ISE) and the square root of the total squared relative error (in percent), also called the root mean square (RMS) relative error, may be used to quantify the error of the approximations, where

$$\text{ISE} = 10 \log_{10} \left(\frac{1}{2\pi} \int_{-\omega\text{max}}^{+\omega\text{max}} \left[\Phi_s^T(\omega) - \Phi_s^K(\omega) \right]^2 d\omega \right) \tag{4.1}$$

and

$$\text{RMS} = 100 \left(\frac{1}{2\pi} \int_{-\omega\text{max}}^{+\omega\text{max}} \left[\frac{\Phi_s^T(\omega) - \Phi_s^K(\omega)}{\Phi_s^T(\omega)} \right]^2 d\omega \right)^{1/2} . \tag{4.2}$$

Table 4.1 presents the ISE and RMS relative error for a variety of cases. The ATSF and AZTSF spectra are equal to $1/\bar{x}$ at non-zero frequencies when $T/\bar{x} = 1$, because only one scatterer contributes to the approximation sum. The approximation error is quite large in this case, but will decline as the number of scatterers included in the summation increases.

Insight into the nature of the approximation error may be obtained by considering the $\alpha = 1$, $T = 100$ case. Because α is unity, the PSD of the random process s is flat except for the delta function at the origin, which represents the DC power of the process. The TSF spectrum is therefore flat except for a replication of $W_T^2(\omega)$ at the origin, which has a $\text{sinc}^2(\omega)$ shape. The ZTSF spectrum obviously lacks this feature. The approximation error of the mean ATSF power spectrum for the $\alpha = 1$, $T = 100$ case is shown in Fig. 4.1. The ATSF spectrum does not match the sidelobes of the W_T^2 function in amplitude, so the error appears as a decreasing oscillatory bias.

Table 4.1 Absolute (ISE) and relative (RMS) error of the mean ATSF and AZTSF power spectra.

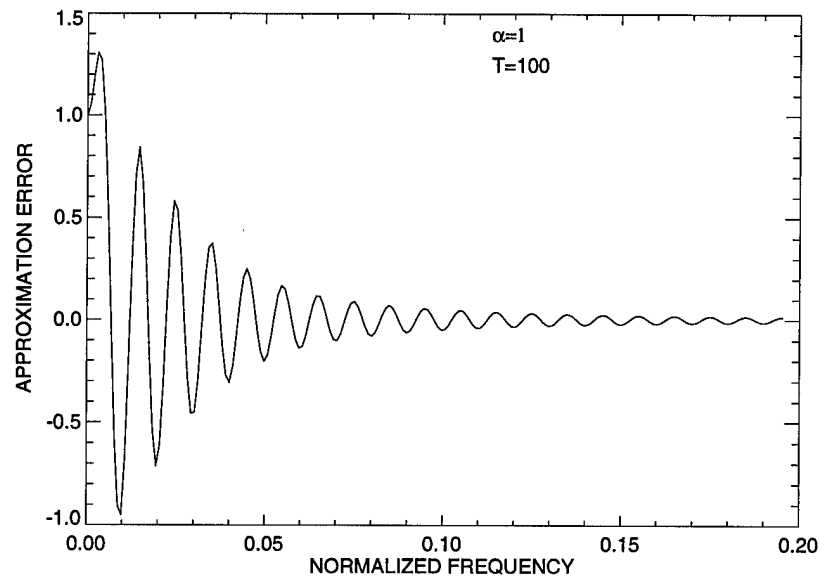| α	T	ATSF		AZTSF	
		ISE (dB)	RMS (%)	ISE (dB)	RMS (%)
10	1	-12.7	24.9	-8.1	87.3
10	10	-24.9	17.8	-27.0	14.3
10	100	-31.1	13.5	-47.0	1.6
10	1000	-36.4	7.5	-67.0	0.2
100	1	-18.2	12.4	-9.3	186.1
100	10	-24.2	8.5	-19.5	62.4
100	100	-41.4	17.1	-38.6	12.6
100	1000	-51.3	14.1	-58.6	1.4
500	1	3.5	76.0	2.9	298.6
500	10	0.8	31.5	0.7	91.7
500	100	-35.8	2.7	-31.7	43.7
500	1000	-54.7	17.8	-51.5	6.7

Figure 4.1 Difference between the mean TSF and ATSF power spectra. Error in tracking $W_T^2(\omega)$ near the origin is dominant for low values if α.

Although the maximum error remains constant as T increases, the ISE and RMS relative error both decline.

The absolute and relative approximation error of the mean ATSF spectrum for the $\alpha = 100$, $T = 100$ case is plotted in Figures 4.2 and 4.3. The error curves demonstrate that there are two types of error: error in approximating the replication of W_T^2 at the origin and error in approximating the higher-frequency harmonic peaks of the TSF spectrum. When α is small relative to $T/\bar{x}$, the approximation error about the harmonic peaks will be biphasic and inversely proportional to T. As α increases, the width of the first harmonic peak of the PSD narrows, becoming equal to the width of W_T^2 when $\alpha \approx 7T/\bar{x}$, so the first peak of the TSF spectrum will take on the character of W_T^2, which the approximation cannot reproduce exactly. The error about the first harmonic peak will therefore increase as α becomes larger than some value, which we take to be approximately $\alpha > 3.5T/\bar{x}$. The inability of the approximation to reproduce W_T^2 also causes the relative error to be large near the origin, although the absolute error is small there. This error declines slower than $1/T$ as T increases.

The absolute and relative approximation error curves for the zero-mean case are presented in Figures 4.4 and 4.5. The comments made concerning approximating the harmonic peaks for the nonzero-mean case also apply here. For the zero-mean approximation, however, the entire error curve appears to diminish as $1/T$. The low-frequency error of this approximation appears primarily as a slowly decreasing bias, rather than the damped oscillatory bias of the nonzero-mean case.

In summary, the quality of the approximation at high frequencies is good unless $T/\bar{x}$ is either very small ($T/\bar{x} < 10$), or small with respect to α, ($T/\bar{x} < \alpha/3.5$). The bias of the approximations at low frequencies, however, causes the RMS relative error to be large even when the higher frequencies are well approximated. In many applications, it is the higher frequency spectral structure that is important, so a bias near the origin would be tolerable. Furthermore, since the absolute error is small at the low frequencies, the performance of algorithms utilizing the ISE as a metric will be insensitive to errors there. The choice between the ATSF and AZTSF approximations
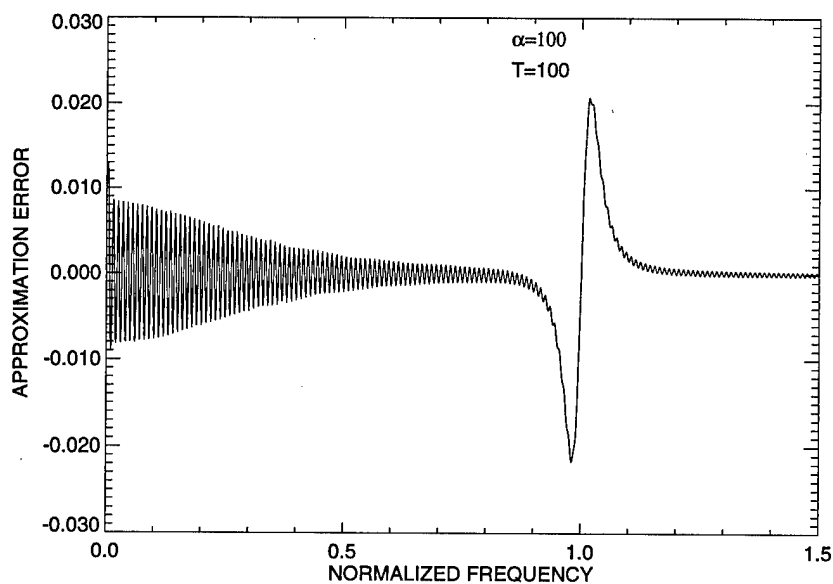
Figure 4.2 Approximation error of the ATSF power spectrum. As α increases, error in reproducing the harmonic peaks dominates the error on an absolute scale.
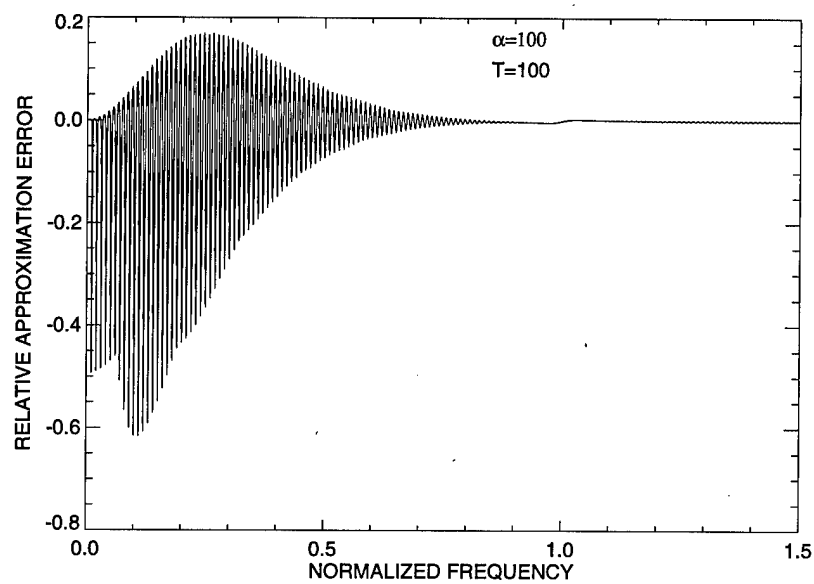
Figure 4.3 Relative approximation error of the ATSF power spectrum.
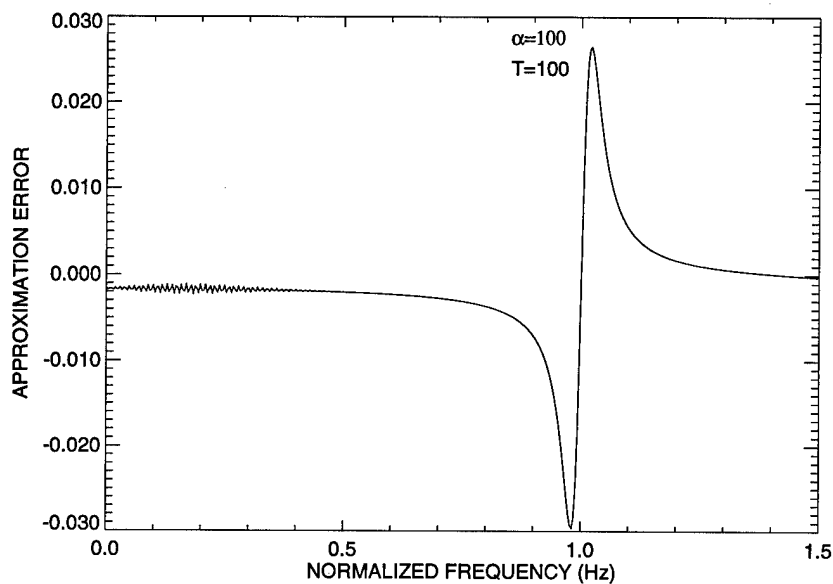
Figure 4.4 Error between the mean ZTSF and AZTSF power spectra. Compare to the nonzero-mean case of Fig. 4.2.
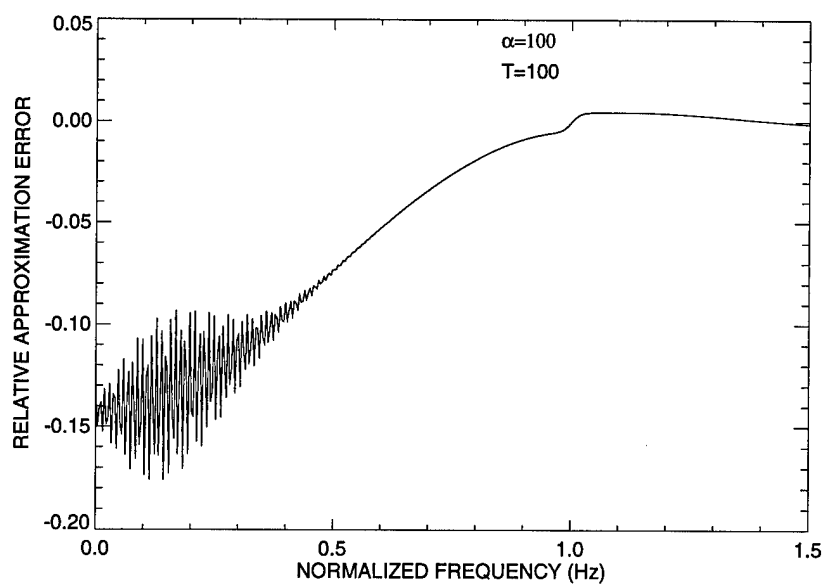
Figure 4.5 Relative error between the mean ZTSF and AZTSF power spectra. Compare to the nonzero-mean case of Fig. 4.3.

should be influenced by the preferred nature of the low frequency error, and the added cost of estimating and removing the mean for the zero-mean case.

We now have expressions that approximate, in closed-form, the mean TSF power spectrum for which the sample mean power spectrum, or periodogram, is an unbiased and consistent estimator [18]. The periodogram may be simulated by generating sample points from the stationary renewal process (SRP) and using those falling in the i-th sample interval to compute the sample TSF power spectrum, $|S_T^i(\omega; \alpha, \bar{x})|^2 / T$. The results for N trials are then averaged to compute the periodogram,

$$\Phi_s^N(\omega; \alpha, \bar{x}, T) = \frac{1}{NT} \sum_{i=1}^{N} \left| S_T^i(\omega; \alpha, \bar{x}) \right|^2. \tag{4.3}$$

In most cases, the sample TSF spectra are exponentially distributed at all frequencies (as a consequence of the central limit theorem), and the signal-to-noise power ratio (SNPR) of the periodogram is equal to N, where the SNPR is the ratio of the squared-mean to the variance. If there are relatively few scatterers in the interval ($T/\bar{x} \le 10$) and the inter-scatterer variance is small (α is large), then the sample spectra will become significantly non-exponential in small intervals about the largest harmonic peaks of the TSF power spectrum, and the SNPR will actually be larger there. The periodogram SNPR must be very large in order for the higher-frequency approximation error to dominate the periodogram noise, a property which extends the useful range of the approximations. For example, a typical ISE for the SNPR = 30dB, $\alpha = 100$, $T = 100$ periodogram is -23dB, whereas the ISE of the ATSF above 0.82 Hz is -46.6 dB. The resolution of the periodogram is approximately $1/T$ (Hz), so the periodogram cannot resolve the peaks of the TSF spectrum if $T/\bar{x}$ is close to unity.

We conclude this chapter by briefly examining the effect of choosing to simulate an ordinary renewal process (ORP) instead of a stationary one. Since we assume that our measurements are truncations of stationary processes, the SRP model is a natural one to use. The distribution of the first arrival time (2.6) must be different from that of the inter-arrival times in a SRP, but, in an ORP model, they are the same. The effect of differing first arrival time distributions on the TSF spectrum

will be negligible when the number of scatterers in the interval is large. Also, when $\alpha = 1$ the two processes are equivalent, so there will be no difference between the TSF spectra. As the average number of scatterers in the interval becomes small, however, the differences become significant. Figure 4.6 compares a simulated periodogram for an ORP (with approximately ten scatterers falling in the sample interval), and the ATSF spectrum for the SRP. The ORP spectrum is biased downward with respect to the SRP spectrum. The bias is explained by noting that the first arrival time of the ORP has a larger mean than that of the SRP, so fewer scatterers fall in the sample interval, on average. When $T/\bar{x}$ becomes unity and α becomes large, the first scatterer of the ORP model will fall near the end of the sample interval, falling inside about half the time, in which case the high-frequency limiting value of the spectrum is one-half that of the SRP. Some analyses have used ORP simulations where SRP ones should have been used [11], and in others the type of simulation used is ambiguous [2].
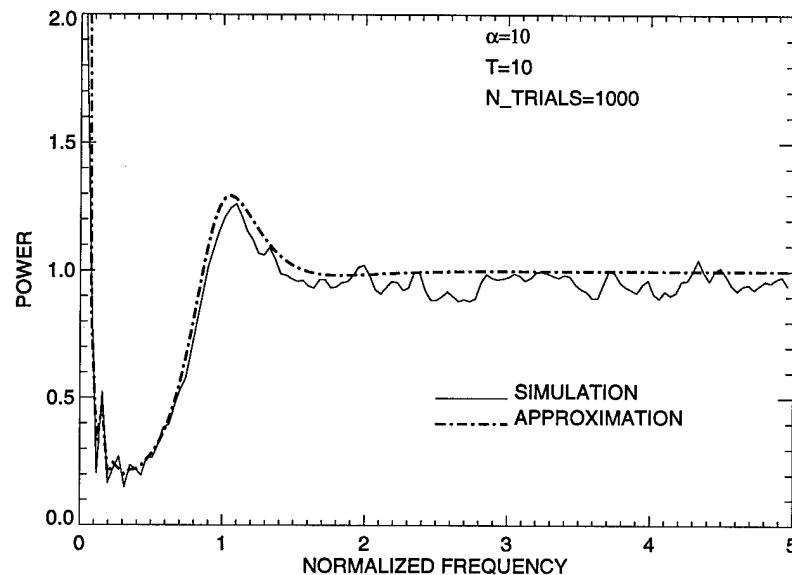

Figure 4.6 Simulated ORP-TSF and ATSF power spectra for a moderately regular surface and a moderately short sample interval.

5. MODEL PARAMETER ESTIMATION

This chapter discusses the problem of finding estimators for the parameters (α, β), or, equivalently, $(\alpha, \bar{x})$, of the regularity model. The sample interval is usually known. Landini and Verrazzani [2] developed one method for extracting the parameters from data measurements. After estimating Φ_s with the periodogram, they estimated $\bar{x}$ by measuring the spacing between peaks in the autocorrelation of the cepstrum. α was estimated by measuring the damping of the autocorrelation. They were able to verify that the parameter estimates agreed, in a gross sense, with the histological characterization of the measured tissues. Despite this agreement, their estimation procedure lacks any form of optimization, so the estimates cannot be described as optimal in any sense. It would be preferable to develop estimators which are either optimal or at least contain an optimization step which can be used to assess the performance of the algorithm.

If the system resolution is fine enough to allow the resolution of the locations of individual scatterers, the maximum-likelihood (ML) solution can be used to estimate the model parameters from the observed inter-arrival times [12]. A sufficient statistic for the unknown parameters, $\vec{\theta} = [\alpha, \bar{x}]$, of the regularity model is $\vec{t}(\vec{x}) = [\sum_1^N x_i, \sum_1^N \ln x_i]$, assuming N samples of the inter-arrival times are available. The ML estimate of $\bar{x}$ is simply the sample mean $\hat{\bar{x}} = \sum_1^N x_i / N$. The ML estimate of α is the solution of

$$\log \hat{\alpha} - \psi(\hat{\alpha}) = \log \hat{\bar{x}} - \sum_{i=1}^N \log(x_i)/N, \tag{5.1}$$

where $\psi(\alpha)$ is the digamma function, $\psi(x) = d \log \Gamma(x)/dx$.

If the scatterers can not be resolved, however, the inter-arrival times cannot be observed. Since the measurements are a somewhat complicated function of the $\{\tau_i\}$, neither the sufficient statistic nor its conditional expected value can be computed,

so neither ML estimation nor expectation-maximization algorithms [19, 20, 21] are feasible.

The problem of estimating $(\alpha, \bar{x})$ from diverse wideband frequency measurements can be formulated as an optimization problem in which we seek to minimize an error metric subject to the constraints that $\alpha > 0$ and $\bar{x} > 0$. Using a squared-error criterion, we may define the total squared error (TSE) to be a function of the true parameters, $(\alpha, \bar{x})$, and the estimated parameters, $(\hat{\alpha}, \hat{\bar{x}})$:

$$\epsilon(\alpha, \bar{x}, \hat{\alpha}, \hat{\bar{x}}; T) = \int \left(\Phi_s^T(\omega; \alpha, \bar{x}) - \Phi_s^T(\omega; \hat{\alpha}, \hat{\bar{x}}) \right)^2 d\omega. \tag{5.2}$$

The total residual error (TRE),

$$e_T = \sqrt{\left(\frac{\alpha - \hat{\alpha}}{\alpha} \right)^2 + \left(\frac{\bar{x} - \hat{\bar{x}}}{\bar{x}} \right)^2}, \tag{5.3}$$

measures the combined error of the parameter estimates. The TSE is a non-negative function with at least one minimum of zero when $(\hat{\alpha}, \hat{\bar{x}}) = (\alpha, \bar{x})$. The complexity of Φ_s^T makes it difficult to prove that (5.2) has a unique global minimum, although in practice we have found this to be the case whenever (5.2) is approximated as a sum over a sufficiently dense set of frequencies.

The mean TSF spectrum for the parameter estimates, $\Phi_s^T(\omega; \hat{\alpha}, \hat{\bar{x}})$, may be evaluated using the convolution (3.7), or approximated by $\Phi_s^K(\omega; \hat{\alpha}, \hat{\bar{x}}, T)$. The actual TSF power spectrum, $\Phi_s^T(\omega; \alpha, \bar{x})$, is estimated from data measurements using the periodogram. When using the ATSF spectrum and the periodogram, we denote the approximate TSE (ATSE) as

$$e_P(\alpha, \bar{x}, \hat{\alpha}, \hat{\bar{x}}; T, N) = \sum_{\omega_i} \left(\Phi_s^N(\omega_i; \alpha, \bar{x}, T) - \Phi_s^K(\omega_i; \hat{\alpha}, \hat{\bar{x}}, T) \right)^2. \tag{5.4}$$

The parameter estimate minimizing (5.4) is denoted $(\hat{\alpha}^\star, \hat{\bar{x}}^\star)$. Since Φ_s^N is an unbiased and consistent estimator of Φ_s^T, the mean of the ATSE will converge to the total squared error between $\Phi_s^T(\omega; \alpha, \bar{x}, T)$ and $\Phi_s^K(\omega; \hat{\alpha}, \hat{\bar{x}}, T)$, which will be close to ϵ whenever the latter is a good approximation of the former. In this case, the optimization procedure compares the observed sample mean TSF power spectrum with the

ATSF power spectrum, and seeks parameter values that minimize the total squared error between the two. The minimization is over all valid values of the parameters, and therefore requires a search to find the optimal values. Since the optimization matches a sample mean spectrum to its (approximate) ensemble-averaged value, this is a moment-matching algorithm [22], and we refer to this estimation scheme as the *moment-matching* method. The algorithm can potentially estimate the model parameters using only a sparse set of frequency measurements, which can reduce the computational requirements and provide insight into the use of sparse narrow-band measurements.

Parameter estimation using this approach will be feasible only if the coordinates of the global minimum of the ATSE surface are close to the true parameters and if the global minimum can be easily located. Plots of (5.4) indicate that the ATSE will have a unique global minimum if the SNPR is large and the frequency samples $\{\omega_i\}$ are sufficiently dense, but we have not proven this. In general, for an arbitrary choice of $\{\omega_i\}$, (5.4) will *not* have a unique global minimum. In order to explore the topic further, we will assume that the $\{\omega_i\}$ will be a set of uniformly spaced frequencies within the interval $(0, 2\pi f_{\max})$, where $f_{\max}$ is chosen to be large enough to include essentially all of the spectral structure of Φ_s^T. From an empirical analysis, $f_{\max} = \max(0.56\alpha^{0.49}/\bar{x}, 2.4/\bar{x})$ (Hz) corresponds to a frequency bandwidth allowing Φ_s to settle to within 1% of its final value of $1/\bar{x}$. The performance of a particular optimization algorithm can then be measured by averaging the TRE of its parameter estimates over many trials (realizations of the point process), and the dependence on the phase of the samples can be suppressed by randomizing the sampling phase over one frequency step for each trial. Since we do not wish to analyze a particular algorithm, we will discuss the structure of the ATSE surfaces and suggest an optimization strategy, but we will then focus on the accuracy and accessibility of the minimum of the ATSE surface.

Fig. 5.1 presents a sample ATSE surface. Several slices of this surface parallel to the $\hat{\bar{x}}$ axis are shown in Fig. 5.2. ATSE surfaces for other values of α and $T/\bar{x}$

Figure 5.1 Typical variation of the total squared error between the ATSF and sample mean TSF power spectra when $(\alpha, \bar{x}) = (100, 1)$, $T = 100$ and $N = 1000$.

Figure 5.2 Representative slices through the surface of Fig. 5.1.

Figure 5.3 Typical variation of the total squared error between the ATSF and sample mean TSF power spectra when $(\alpha, \bar{x}) = (1000, 1)$, $T = 100$ and $N = 1000$.

are similar in appearance, as Figs. 5.3 to 5.5 illustrate. The common features of these surfaces are worth noting. Since the ATSF spectrum is a function of $\omega\hat{\bar{x}}$, changing $\hat{\bar{x}}$ stretches or compresses the ATSF spectrum with respect to the frequency axis. As $\hat{\bar{x}}$ grows large, the ATSF spectrum compresses towards the origin and its high frequency limiting value of $1/\hat{\bar{x}}$ approaches zero, so the ATSE becomes the total power of $\Phi_s^N(\omega)$. As $\hat{\bar{x}}$ becomes less than $\bar{x}$, the ATSE rises sharply, but then declines when the maximum of Φ_s^K at $f = 1/\hat{\bar{x}}$ moves outside of the frequency range of interest. Although it is not shown in the ATSE figures, as $\hat{\bar{x}}$ becomes even smaller, the error will rise again because the lobe of Φ_s^K centered at the origin will increase in magnitude until it overlaps with the maxima of Φ_s^N.

If $\hat{\bar{x}}$ is varied when $\hat{\alpha}$ is large, the many extrema of the ATSF spectrum interact with those of Φ_s^N to create multiple extrema in the ATSE, which are apparent in Fig. 5.2. If $\hat{\alpha}$ is chosen so that only the maximum of Φ_s^K at $f = 1/\hat{\bar{x}}$ is developed, this behavior will be suppressed, and the ATSE will vary smoothly with $\hat{\bar{x}}$, except at very
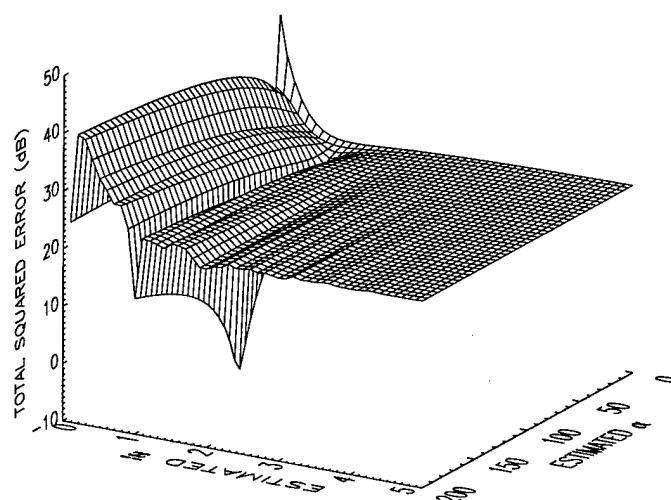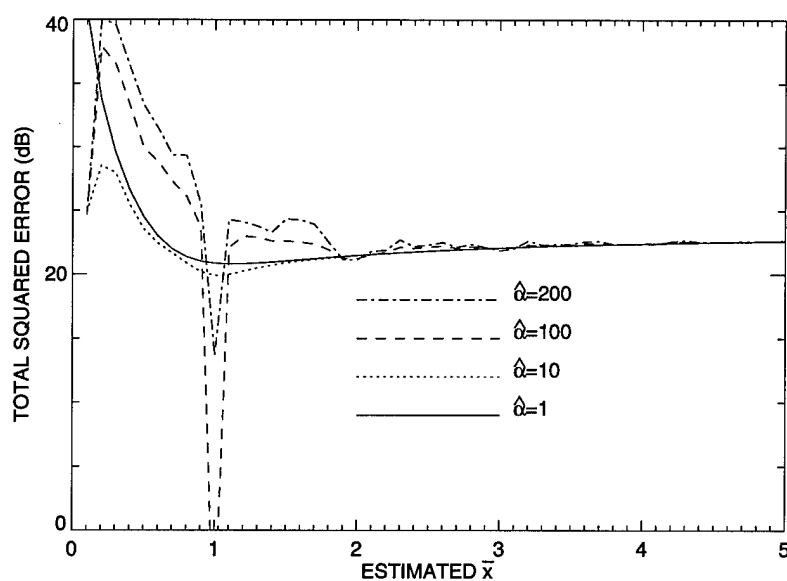
Figure 5.4 Typical variation of the total squared error between the ATSF and sample mean TSF power spectra when $(\alpha, \bar{x}) = (10, 1)$, $T = 100$ and $N = 1000$.

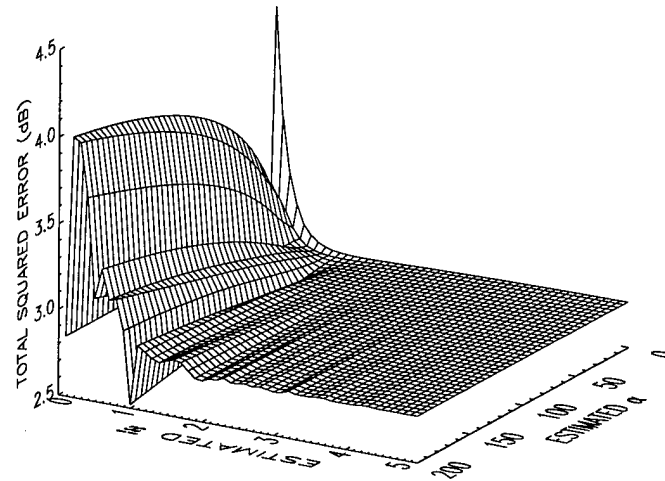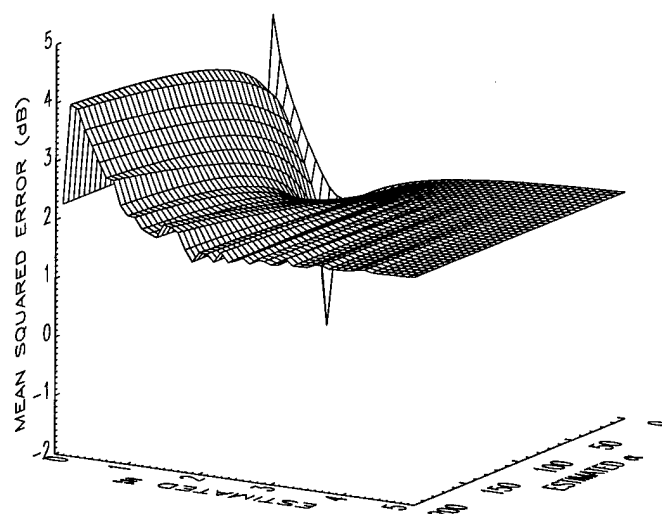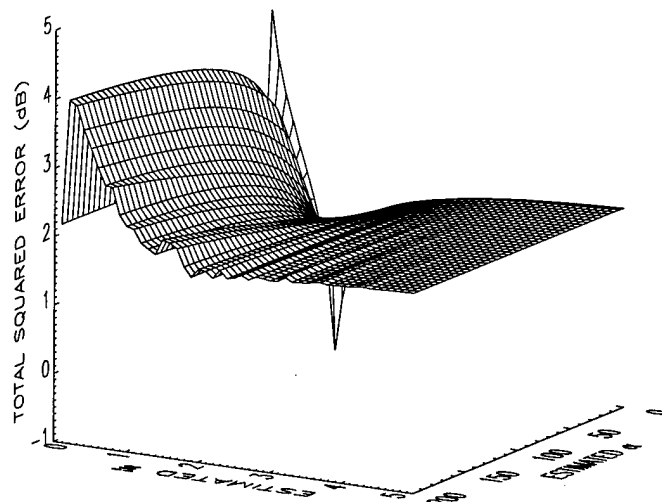Figure 5.5 Typical variation of the total squared error between the ATSF and sample mean TSF power spectra when $(\alpha, \bar{x}) = (1, 1)$, $T = 100$ and $N = 1000$.

small values. If $\hat{\alpha} = 1$, Φ_s^K is a constant equal to $1/\hat{\bar{x}}$, and so the ATSE grows as $1/\hat{\bar{x}}$ as $\hat{\bar{x}}$ decreases. The ATSE varies smoothly with $\hat{\alpha}$.

We have exploited the behavior of the ATSE function for this hypothetical scenario to demonstrate that it is possible to design a parameter search algorithm for the moment-matching method that is relatively immune to the problem of becoming trapped at local minima. We initially optimize with respect to $\hat{\bar{x}}$ with $\hat{\alpha} = 10$, because the ATSE behaves relatively well when only the $f = 1/\hat{\bar{x}}$ maximum of Φ_s^K is developed. Given this optimal $\hat{\bar{x}}$, an optimization with respect to $\hat{\alpha}$ will produce a set of parameter estimates in the neighborhood of the global minimum, because the ATSE varies smoothly with $\hat{\alpha}$. A search scheme such as gradient descent can then be used to accurately locate the global minimum; we successfully used the IMSL routine DBCONF [23]. The default stopping parameters were used, with the exception of the gradient tolerance, which was chosen to be 0.001. We found that adequate results could also be obtained using a simple univariate search, which alternates between searching for α and $\bar{x}$ by using a simple bisection algorithm [24] which halves the

Table 5.1 Average TRE (%) of $(\hat{\alpha}^{\star}, \hat{\bar{x}}^{\star})$ for the ATSE function with SNPR $= \infty$, averaged over 100 trials with random sample phases. Each box is of the form: sample mean/standard deviation.

	$\alpha = 1$	2	5	10	20	50	100	200	500
$T = 2$	97.5/3.8	76.9/2.4	9.2/1.1	11.8/0.4	10.4/0.01	3.0/0.02	1.6/0.002	1.3/0.0004	0.8/0.07
5	29.6/1.6	19.0/3.1	1.9/0.4	2.6/0.06	2.2/0.2	1.3/0.002	0.8/0.06	0.3/0.0002	0.2/0.0001
11	16.4/0.7	11.3/0.8	2.0/0.1	0.7/0.3	0.6/.04	0.7/0.1	0.6/0.04	0.2/0.04	0.03/0.0004
20	6.0/0.9	2.6/2.1	1.6/0.6	0.9/0.1	0.3/0.01	0.2/0.03	0.6/0.01	0.2/0.05	0.02/0.0004
51	3.3/0.3	1.8/1.1	0.3/0.1	0.4/0.2	0.6/0.1	0.1/0.02	0.2/0.008	0.3/0.1	0.08/0.03
111	0.6/0.5	1.3/0.6	1.1/0.2	0.6/0.2	0.9/0.2	0.2/0.1	0.02/0.003	0.1/0.04	0.1/0.07
200	0.3/0.1	1.2/0.6	1.0/0.2	0.5/0.2	0.7/0.2	0.2/0.1	0.1/0.01	–	–

search interval containing the minimum until the slope of the ATSE curve is suitably small (0.001, as before). It is not our intention, however, to analyze the performance of a particular optimization algorithm, but rather to explore the general performance limitations of all such algorithms.

Typically, the coordinates of the minimum of the ATSE surface differ from the true parameter coordinates because the sample mean TSF spectrum is random and the ATSF spectrum is only an approximation to the TSF spectrum. Effects due to the former cause can be eliminated by letting $N \to \infty$ (SNPR $= \infty$), which is equivalent to using a numerical evaluation of the convolution (3.7). For this case, the average TRE due to the approximation is tabulated in Table 5.1. The convolution was calculated by multiplying the discrete Fourier transforms (DFT's) of samples of the functions to be convolved and inverting. In order to be numerically accurate, the sequence lengths may need to be quite long, in which case the computation time becomes significantly longer than that of the ATSF spectrum.

In Chapter 4, we showed that the ATSF spectrum approximation error increased for $\alpha > 3.5T/\bar{x}$ because of error in approximating the harmonic peaks of the TSF spectrum. The performance data of Table 5.1 suggest that this type of approximation error does not have a significant effect on the parameter estimation scheme over the parameter ranges examined. The ATSF approximation error is also large when $T/\bar{x}$ is small, corresponding to the case where few scatterers fall in the sample interval,
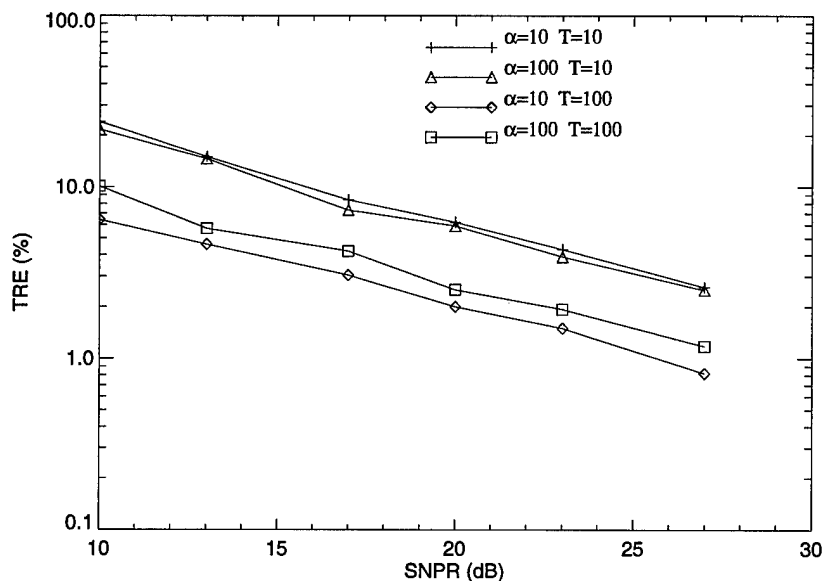
Figure 5.6   Variation of total residual error with periodogram SNPR.

on average. Table 5.1 indicates that this error will adversely effect the parameter estimation error, so the ATSF spectrum should be replaced by the numerical computation of the mean TSF spectrum in certain cases, for example: $T/\bar{x} < 20 - \alpha$. This is convenient, since it is not cumbersome to accurately calculate the convolution in these cases.

The effect of the introduction of periodogram noise on the TRE is demonstrated in Fig. 5.6, for which finite-SNPR periodograms (4.3) are used to estimate the TSF spectrum. The TRE appears to be inversely proportional to the square root of the SNPR, with the constant of proportionality depending on both α and $T/\bar{x}$. This type of behavior indicates that the performance degradation of a search algorithm as SNPR decreases will be gradual. For a given α, the TRE will be smaller for a larger value of $T/\bar{x}$. It is also of interest to notice that the TRE is not dramatically affected as long as NT is held constant.

Since the moment-matching algorithm uses samples of frequency-domain functions, it is necessary to determine how algorithm performance depends upon the

frequency-sampling rate. All of the prior TRE's were calculated using a very dense set of frequencies, which suppressed sampling rate effects. The first peak in the scatterer function PSD (2.13) is the narrowest and corresponds to a single term of Sanderson's expansion (2.18). Various measures of the temporal bandwidth of this term can be defined. The RMS bandwidth, given by

$$B_{\text{rms}} = \frac{\int_0^\infty t^2 e^{-2\alpha_2 t} \cos^2(\omega_2 t)\,dt}{\int_0^\infty e^{-2\alpha_2 t} \cos^2(\omega_2 t)\,dt}, \tag{5.5}$$

where α_2 and ω_2 are defined in (2.16) and (2.17), is approximately $0.05\alpha\bar{x}$ (sec). Another measure is the time at which the term of the autocorrelation function corresponding to the aforementioned term in Sanderson's expansion is reduced by 50%, which is given by $B_{50\%} = 0.035\alpha\bar{x}$ (sec). Another measure is the inverse of the 3-dB width of the first peak of the PSD, which is given by $B_{3\text{dB}} = \pi\bar{x}/\alpha_2 \approx 0.16\alpha\bar{x}$. One might expect that the Nyquist frequency-sampling rate required for adequate representation of Φ_s should be approximately twice whichever of these bandwidth measures is appropriate. Note that all of these measures vary linearly with α.

Since the TSF spectrum is a filtered version of the PSD, its Nyquist frequency-sampling rate should be no greater than that of the PSD. But, since successive peaks have progressively smaller temporal bandwidths, and several peaks are included in the measurement scenario we have assumed, it is not obvious how the TRE is related to the frequency sampling rate. In addition, knowledge of the approximate parametric form, Φ_s^K, of Φ_s^T represents additional information which may reduce the Nyquist sampling requirement. The reduction of the bandwidth of successive peaks as frequency increases suggests that the frequency-sampling rate could be varied, or "chirped", with frequency to improve the sampling efficiency.

As α increases, each peak in the PSD narrows as its amplitude increases. The first peak will therefore become undersampled as α increases, which should cause an increase in TRE. The emergence of higher-order peaks, which have smaller bandwidths, should exert an opposite influence on TRE, so it is difficult to predict how the combination of these two influences should affect TRE.

Figures 5.7 and 5.8 show how the TRE varies with frequency sampling rate,
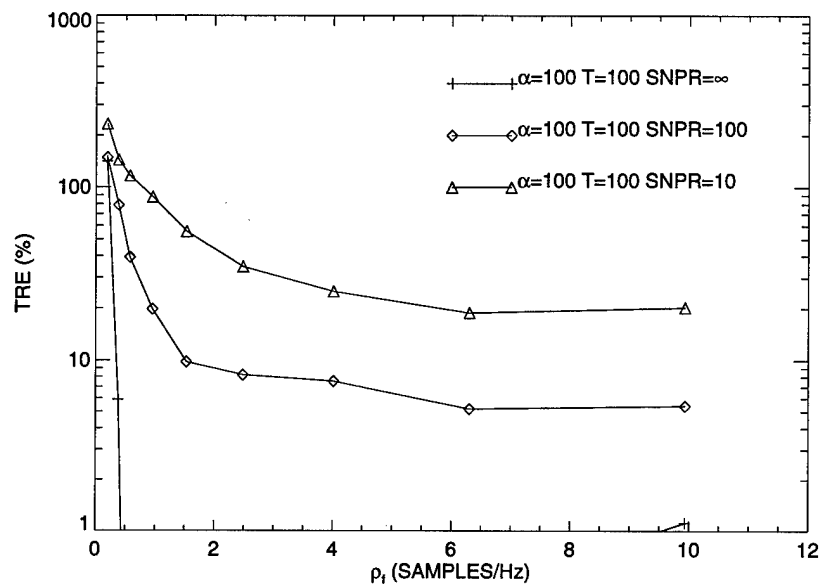
Figure 5.7 Variation of total residual error with the frequency sampling rate for various SNPR values.
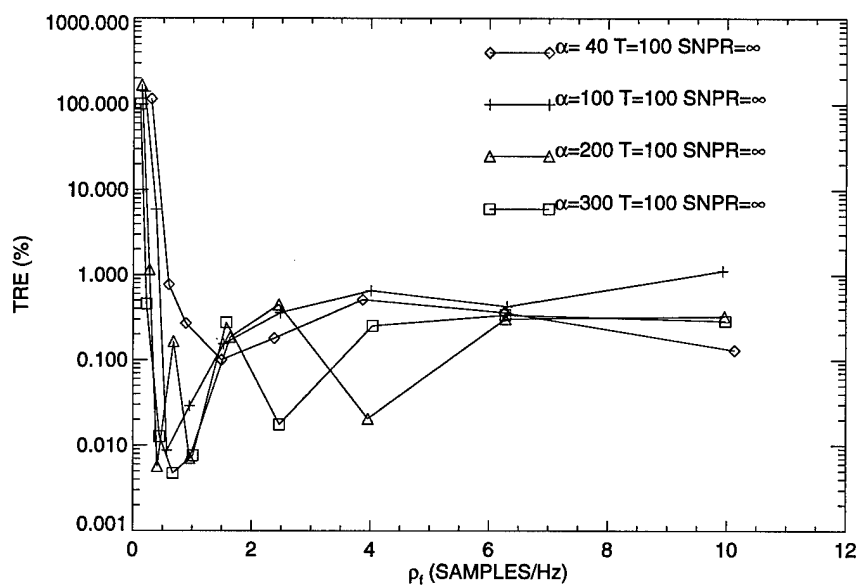
Figure 5.8 Variation of total residual error with the frequency sampling rate for various α values.
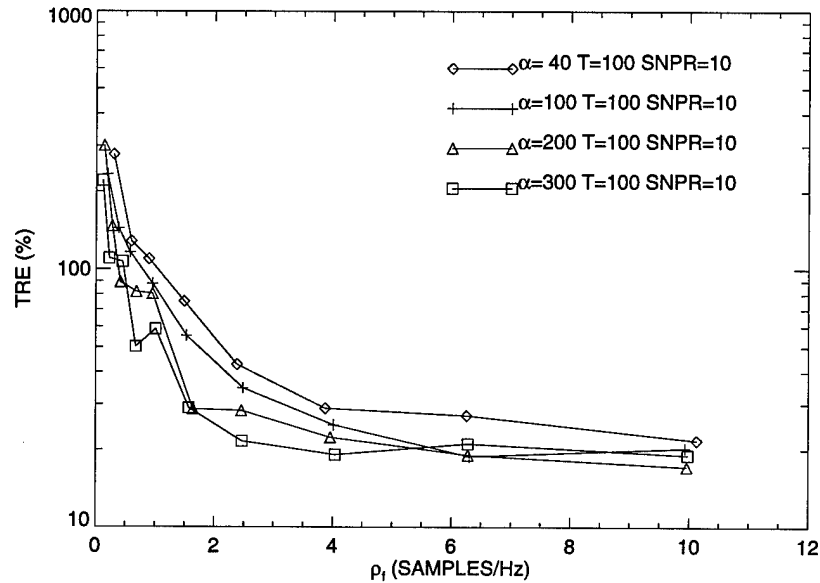
Figure 5.9 Variation of total residual error with the frequency sampling rate for various α values with SNPR = 10.

ρ_f, for various values of SNPR and α. The ratio of the SNPR = 10 and SNPR = 100 curves at larger sampling densities becomes close to the $\sqrt{10}$ factor observed in Fig. 5.6. Extrapolating from the TRE values at the largest sampling density (9.93 samples/Hertz), the SNPR that would produce a TRE equal to that of the SNPR=∞ case would be 1651. This suggests that the TRE would not be improved by increasing the SNPR beyond this approximate value. It also implies that periodogram noise dominates approximation error as a source of TRE unless the SNPR is very large, as we speculated at the end of Chapter 4. Both finite-SNPR curves flatten at approximately 6 (samples/Hz), suggesting an approximate limit beyond which the TRE will not be improved in this case.

Figure 5.8 shows that the TRE for the SNPR=∞ case is large when the sampling density is pathologically small, but it is generally below 1% at other sampling densities for all α. This implies that the coordinates of the global minimum of the ATSE surface are usually very close to the true parameter values when there is no periodogram noise. Figure 5.9 shows the TRE for various α at an SNPR of 10. There is a slight

separation of the curves at this SNPR, with the lowest value of α having the largest TRE. This suggests that, with a finite SNPR, parameter estimation can potentially be more accurate with as α increases, because the coordinates of the global minimum of the ATSE surface are getting closer to the true parameter values.

While TRE measures the error of the coordinates of the global minimum of the ATSE surface, it does not indicate how difficult that minimum may be to locate. We assess this by estimating $P_c = \|S_c\|/\|S\|$, where S is a finite convex subset of the $(\hat{\alpha}, \hat{\hat{x}})$ parameter space and S_c is the subset of S in which a gradient descent algorithm will converge to the global minimum. This ratio represents the a priori probability of convergence if the gradient descent algorithm is started at a random location in S and the sampling phase and point process are generated randomly. In the plots of P_c that follow, S is approximated by a grid with logarithmically-spaced points at a density of 20 per decade. Figures 5.10 and 5.11 show how P_c varies with the frequency sampling rate for various values of SNPR and α. Fig. 5.10 shows that P_c is not strongly affected by the SNPR, which implies that the ability to find the global minimum of the ATSE surface is not critically dependent on SNPR. The P_c curves do shift significantly to the right as α increases, however. This indicates that it becomes more difficult to locate the global minimum of the ATSE surface as α increases. This might be expected, since we expect more local minima to develop in the ATSE surface as α increases. The P_c curves tend to reach a maximum of about 80%. Fitting curves to the P_c data for each α and using them to predict where $P_c = 0.8$, then fitting these points as a function of α yields $\rho_f^{80\%} = 0.0194\alpha + 4.03$ ($r = -.987$), where r is the correlation coefficient of the linear-least squares fit; values of r close to unity indicate a better fit. This is a rather crude estimate of the frequency sampling rate required to maintain P_c at a reasonably large value. The linear dependence on α is similar to that of the temporal bandwidth measures observed earlier; the smallest of the Nyquist rates suggested by these measures is 0.08α. This sampling rate is comparable to $\rho_f^{80\%}$ for small α, but becomes larger as α increases. This implies

Figure 5.10 Variation of the probability of convergence with the frequency sampling rate for various SNPR values.

Figure 5.11 Variation of the probability of convergence with the frequency sampling rate for various α values.
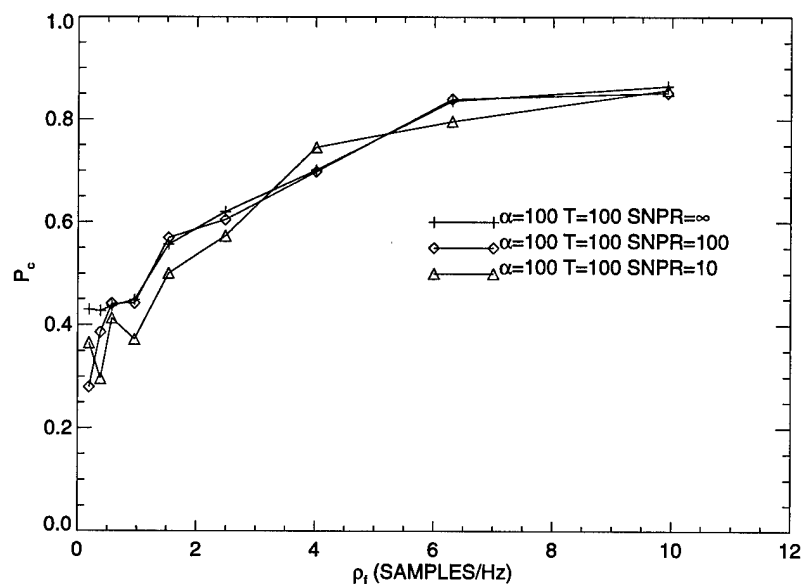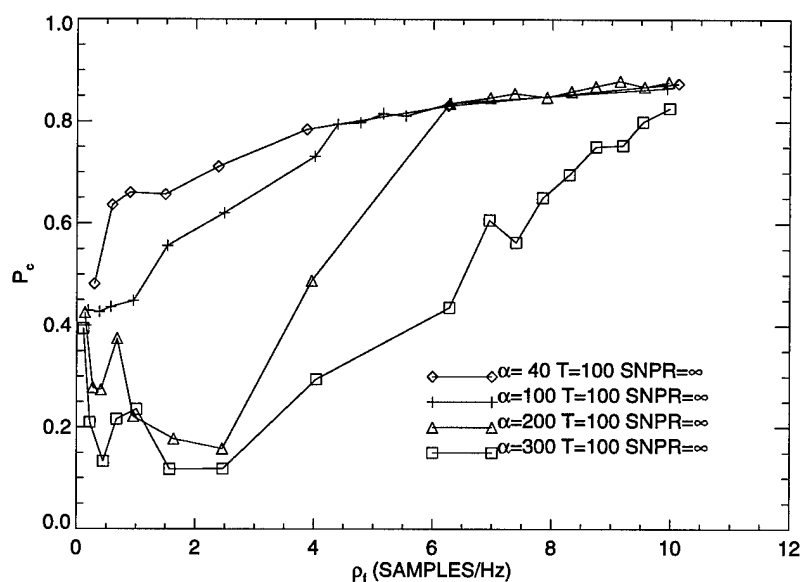
that the frequency sampling rate required for feasible parameter estimation can be significantly less than the Nyquist rate suggested by the spectral structure.

6. MARKED POINT PROCESS MODELS

The regularity model, until this point, has only allowed scatterers with unit reflectivity. In this chapter, this restriction is lifted and the more realistic assumption of random reflectivity is applied. The stationary renewal process with non-unit-magnitude points is called a marked point process, where the reflectivity of the point is the mark associated with that point. We assume that the marks form a stationary random process that is independent from the stationary renewal process, and characterize the mark process with its second-order statistics. Two scenarios are possible: the marks may be sequentially correlated or temporally correlated. The autocorrelation of temporally correlated marks is a function of the time separation between the marks, while that of sequentially correlated marks is a function of the difference of the sequentially numbered indices of the marks.

6.1 Temporally Correlated Marked Point Processes

The temporally correlated case can be modelled as the product of the original scatterer function and the mark process, $m(t)$:

$$s_{mt}(t) = m(t)s(t). \tag{6.1}$$

and the power spectrum of the marked process is the convolution of those of the mark process and the scatterer function:

$$\begin{aligned}
\Phi_{smt}(\omega) &= \Phi_m(\omega) \star \Phi_s(\omega). \\
&= \Phi_{\overline{m}} \star \Phi_s + \overline{m}^2 \Phi_s, \tag{6.2}
\end{aligned}$$

where $\Phi_{\overline{m}}$ is the PSD of the zero-mean mark process. The latter form shows that the PSD is the summation of the original PSD (weighted by the square of the mean of

the marks) with a filtered version of itself (which will be proportional to the variance of the marks).

We once again assume that the system impulse response varies smoothly with respect to $\Phi_{smt}(\omega)$ and is broadband with respect to $W^2(\omega)$, and that we may compensate for its effects. The marked temporally-correlated truncated scatterer function (MTTSF) power spectrum is then

$$\Phi^T_{smt}(\omega) = \Phi_s(\omega) \star \Phi_m(\omega) \star W^2_T(\omega)/T, \qquad (6.3)$$

so the mark process acts in the same capacity as a window function. Although (6.2) and (6.3) provide intuitive insight into the effect of the marks, they have no closed-form equivalents.

If the power spectrum of the mark process is narrowband with respect to the window spectrum W^2_T, the marks will not affect the TSF spectrum substantially. This would be the case when the correlation length of the marks is longer than the window length T. The marks would be expected to exert a more substantial effect on the TSF spectrum as their correlation length becomes shorter than the data window. In the limit, if the marks are completely uncorrelated, $\Phi_m(\omega)$ becomes flat and obscures all the spectral structure in $\Phi_s(\omega)$.

We can define the autocorrelation of the mark process to be

$$\phi_{mt}(t) = \sigma^2_m \rho_{mt}(t) + \overline{m}^2, \qquad (6.4)$$

where $\rho_{mt}(t)$ is the normalized autocovariance function, and $\overline{m}$ and σ^2_m are the mean and variance, respectively, of the mark process.

If we assume that the form of the autocovariance is

$$\rho_{mt}(t) = e^{-|t|/\tau_{mt}} \cos(\omega_{mt} t), \qquad (6.5)$$

a closed-form expression may be derived for the mean ATSF spectrum. Examples of signals that can be modelled with this autocovariance include the output of single degree-of-freedom systems, such as a simple damped spring-mass, with white noise

input [25], or the output of a narrow-band bandpass filter with wideband noise input [26]. This autocorrelation, with $\omega_m = 0$, also describes binary signals with switching times generated by a Poisson process [26], and the output of a first-order low pass (R-C) filter. The Ornstein-Uhlenbeck solution of Langevin's equation, which describes the velocity of motion of a particle undergoing free Brownian motion with white Gaussian input noise, also has an autocorrelation of this form [27].

The independence of $m(t)$ and $s(t)$ allows us to write

$$\Phi_{smt}^K(\omega) = \frac{1}{T} \sum_{m=1}^K \sum_{n=1}^K E\left\{\phi_{mt}(T_m - T_n)e^{\jmath\omega(T_m-T_n)}\right\}. \tag{6.6}$$

Proceeding as in the case of the ATSF derivation, the sum is split into the cases of $m = n$, $m > n$ and $m < n$, and we use the identities (3.14), (3.16), and (3.18) to write

$$\Phi_{smt}^K(\omega) = \overline{m}^2\Phi_s^K(\omega) + \frac{\sigma_m^2}{T}\left(K + \Re\{G(Z_{t1}) + G(Z_{t2})\}\right), \tag{6.7}$$

where

$$Z_{t1} = (1 + \beta/\tau_{mt} + \jmath\beta(\omega + \omega_{mt}))^\alpha, \tag{6.8}$$

$$Z_{t2} = (1 + \beta/\tau_{mt} + \jmath\beta(\omega - \omega_{mt}))^\alpha. \tag{6.9}$$

This function is the sum of the unmarked ATSF spectrum, weighted by the square of the mean of the marks, and a new expression that is weighted by the variance of the marks. We will refer to (6.7) as the mean MTATSF spectrum, where "MT" denotes the marked temporally-correlated case.

6.2 Sequentially Correlated Marked Point Processes

The sequentially correlated marked process may be written as

$$s_{ms}(t) = \sum_n m_n\delta(t - T_n). \tag{6.10}$$

In this case, there is no equivalent to the intuitively-pleasing open form of (6.2), but a closed-form expression for the PSD can be derived for specific mark autocorrelation functions.

The general form of the PSD was derived by Leneman [13] and is given by:

$$\Phi_{sms}(\omega) = \frac{\phi_{ms}(0)}{\bar{x}} + \frac{1}{\bar{x}} \sum_{n=1}^{\infty} \phi_{ms}(n)(F(\omega)^n + F(-\omega)^n).$$ (6.11)

Again assuming an exponentially damped form for the autocovariance,

$$\rho_{ms}(n) = e^{-|n|/\tau_{ms}} \cos(\omega_{ms} n),$$ (6.12)

the geometric series can be evaluated to produce

$$\Phi_{sms}(\omega) = \overline{m}^2 \Phi_s(\omega) + \frac{\sigma_m^2}{2\bar{x}} \left[\frac{|Z_{s1}|^2 - 1}{|Z_{s1} - 1|^2} + \frac{|Z_{s2}|^2 - 1}{|Z_{s2} - 1|^2} \right],$$ (6.13)

where

$$Z_{s1} = Z e^{1/\tau_{ms}} e^{-\jmath \omega_{ms}}$$ (6.14)

$$Z_{s2} = Z e^{1/\tau_{ms}} e^{\jmath \omega_{ms}}.$$ (6.15)

As in the temporal case, the PSD is the weighted sum of the unmarked PSD and a modified expression.

Given the same assumptions about the system response as in the temporally correlated case, the truncated scatterer function power spectrum can be written as

$$\Phi_{sms}^T(\omega) = \Phi_{sms}(\omega) \star W_T^2(\omega)/T.$$ (6.16)

A closed-form expression may be derived for the mean ATSF spectrum. Proceeding as in the temporally-marked case, the independence of $m(n)$ and $s(t)$ allows us to write

$$\Phi_{sms}^K(\omega) = \frac{1}{T} \sum_{m=1}^{K} \sum_{n=1}^{K} \phi_{ms}(m - n) E \left\{ e^{\jmath \omega(T_m - T_n)} \right\}.$$ (6.17)

Using (3.14), (3.16) and (3.18), this becomes

$$\Phi_{sms}^K(\omega) = \overline{m}^2 \Phi_s^K(\omega) + \frac{\sigma_m^2}{T} \left(K + \Re\{G(Z_{s1}) + G(Z_{s2})\} \right).$$ (6.18)

We will refer to (6.18) as the mean MSATSF spectrum, where "MS" denotes the marked sequentially-correlated case.

6.3 General Observations

All of the PSD or ATSF expressions show the marked spectra to be the sum of the unmarked spectra, weighted by the square of the mean of the marks, and a new expression that is weighted by the variance of the marks. If the signal-to-mark-noise power ratio (SMNPR), $\overline{m}^2/\sigma_m^2$, is large, the marks will not alter the PSD or ATSF expressions significantly, and so the marks can be ignored.

Assuming that $\omega_m = 0$, the temporal and sequential cases should be equivalent when the number of temporally-correlated scatterers falling within one correlation length, $N_{\tau_{mt}}$, is equal to the number of sequentially-correlated scatterers, τ_{ms}. This will be the case when the variance of $N_{\tau_{mt}}$ is relatively small, which is true when α is large or τ_{mt} is large; in these cases $N_{\tau_{mt}}$ is close to its mean value of $\tau_{mt}/\bar{x}$. Comparisons of the MTATSF and MSATSF spectra verify this behavior.

The form of the temporally-correlated TSF spectrum (6.3) shows that the marks will only affect the spectrum if the correlation length is not large with respect to T. Although there is no equivalent to (6.3) in the sequentially correlated case, the relationship between the window length and the correlation length, $\tau_{ms}\bar{x}$, should be similar. In the extreme case where the marks are uncorrelated, the marks contribute a constant term to the PSD of the marked process, so the marks act to obscure the spectral structure of the scatterer process.

7. APPROXIMATION ACCURACY IN THE MARKED CASE

Just as in the unmarked case, the approximation error of the marked ATSF expressions may be analyzed by comparing them to numerical evaluations of the TSF spectra for various parameter combinations. Both the marked TSF and marked ATSF spectra may be separated into terms due to the unmarked and marked processes; the accuracy of the former was discussed earlier. The accuracy of the latter terms may be examined by setting $\overline{m} = 0$ and $\sigma_m^2 = 1$ and comparing the ATSF spectra with numerical evaluations of (6.3) and (6.16). Table 7.1 presents the error between these functions for the temporally correlated case in both the ISE and RMS forms, for various extremes of parameter values. The values of correlation length were chosen to be either $T/10$ or $10T$. Since the temporal and sequential cases can be made approximately equivalent through the appropriate choice of parameters, only the temporal case is considered here.

The table indicates that the error increases with τ_m and decreases with T and α. As the correlation length becomes longer, the contribution of the marks looks more like the original unmarked process spectrum, and, in fact, these terms become equivalent to the unmarked ATSF spectrum in the limiting case. For large τ_m, then, the error is that of the unmarked case, which can be verified by comparing this table with Table 4.1. Relatively small errors are associated with small values of τ_m. Since (6.3) shows that the effect of the mark process is to filter the unmarked process, the mark components of the TSF spectrum should appear to be smoothed versions of the unmarked TSF spectrum. The small error associated with small values of τ_m then indicates that the functional form of the MTATSF spectrum is a better approximator of these smoothed spectra than the ATSF function was of the unsmoothed spectra.

Table 7.1 Absolute(ISE) and relative (RMS) error of the MTATSF power spectrum.

α	T	τ_m	ISE (dB)	RMS (%)
10	10	1	-37.3	1.8
10	10	100	-25.4	18.4
100	10	1	-43.1	1.0
100	10	100	-24.2	9.4
10	100	10	-47.9	0.4
10	100	1000	-31.8	14.4
100	100	10	-47.5	0.2
100	100	1000	-41.6	17.4

The approximation accuracy of the marked ATSF spectra is therefore dominated by that of its unmarked ATSF spectral component, so the extension of the ATSF expressions to the marked case adds very little extra approximation error. Accurate evaluations of the marked TSF convolution (6.3) can become costly, because the tails of the autocorrelation function or its PSD can lead to aliasing errors. In these instances, the closed-form approximations provided by the MTATSF and MSATSF spectra can be quite valuable.

8. PARAMETER ESTIMATION WITH MARKED PROCESSES

At a minimum, the mark process adds three new parameters, $\overline{m}$, σ_m^2 and τ_m, to the two characterizing the regularity model. In order to restrict the scope of the investigation, we will not consider mark models with nonzero ω_m. The significance of the marks depends only on the SMNPR, so we shall assume that $\overline{m}$ has been normalized to unity. The presence of the marks in the parameter estimation problem can be viewed in two ways. One can assume that the parameters characterizing the mark process simply increase the dimensionality of the estimation problem by replacing the unknown parameter vector $\vec{\theta} = [\alpha, \bar{x}]$ with $\vec{\theta} = [\alpha, \bar{x}, \sigma_m^2, \tau_m]$, or one can view the marks as noise which interferes with the estimation of the original regularity model parameters.

We consider the former case first. It is difficult to examine the limitations on estimator performance with the same level of detail as was done in the two-parameter case because the computational costs increase exponentially with the dimensionality of the problem. In the original two-dimensional problem, P_c was approximated by evaluating the ATSE on a mesh of points and then determining which of these points was in the set which converged to he global minimum. In four dimensions, it was computationally prohibitive to compute the ATSE on a similar four-dimensional mesh, so the mesh density was reduced to four points per decade. In order to gauge the effect of the marks on parameter estimation, we first examine some representative cases in which the frequency sampling rate is chosen to be large enough to not be an issue. We consider only the temporally correlated process, since the temporal and sequential cases can be made approximately equivalent with the appropriate choice of parameters. Table 8.1 shows the TRE of the global minimum of the ATSE surface for various mark parameters and a fixed set of regularity model parameters. The

Table 8.1 Average TRE (100 trials) for various combinations of mark parameters with $\alpha = 40$, $T = 100$, and SNPR=∞. TRE entries are of the form: mean/standard-deviation. Averages of individual parameter errors are also shown.

σ_m^2	τ_m	TRE (%)	e_α	$e_{\bar{x}}$	$e_{\sigma_m^2}$	e_{τ_m}
0.1	100	84/94	0.06	0.03	0.2	39.0
1	100	12/14	0.02	0.03	0.05	2.0
10	100	4/4	0.02	0.03	0.03	1.0
0.1	10	45/170	0.02	0.01	3.7	21.1
1	10	5/9	0.08	0.02	0.21	0.5
10	10	0.7/1	0.01	0.03	0.01	0.3
0.1	1	93/240	0.4	0.06	2.6	59.6
1	1	8/15	1.05	0.05	0.27	4.4
10	1	1/3	0.2	0.0001	0.007	0.2
0.1	0.1	119/78	0.6	0.2	5.1	45.6
1	0.1	118/120	0.5	0.07	0.02	79.6
10	0.1	85/135	0.3	0.03	0.002	72.7

table also shows the averages of the individual component errors. The algorithm used to locate the global minimum of the ATSE often failed to converge when τ_m was small (0.1), resulting in a large TRE. This is because the gradient of the ATSE surface rapidly decreases to zero in the direction of decreasing $\hat{\tau}_m$, when $\hat{\tau}_m < \tau_m$. This behavior becomes more severe as τ_m decreases. An intuitive explanation is that once the correlation length becomes less than one mean inter-scatterer distance, it becomes impossible to distinguish between estimated correlation lengths that are less than one mean inter-scatterer distance.

The TRE in all cases of Table 8.1 was dominated by error in estimating the correlation length, which may be seen by examining the averages of the individual parameter estimation errors. The TRE decreases as σ_m^2 increases, indicating that the mark parameters are difficult to estimate when the marks are not significant. On the other hand, it appears that α and $\bar{x}$ can still be accurately estimated, even when the marks are significant and regardless of the correlation length.

If the marks are viewed as a noise which corrupts the measurement of the fundamental scatterer process, the goal of a parameter estimation scheme, as it was in the unmarked case, is to estimate $\vec{\theta} = [\alpha, \bar{x}]$. In this case, the parameters can be estimated by trying to minimize the ATSE in four dimensions between the observed marked spectrum and the MTATSF or MSATSF spectra, or the error may be minimized in only two dimensions using the unmarked ATSF spectrum. The SMNPR now has the interpretation of being a true signal-to-noise ratio. The data of Table 8.1 indicate that the former approach can be quite successful, since the average error of the α and $\bar{x}$ estimates is small.

The feasibility of the latter approach may be examined by determining P_c and TRE for the two-dimensional ATSE surface which is generated by differencing the MTTSF and ATSF spectra. In this case, the estimation procedure minimizes the error between the marked-process TSF spectrum and the unmarked ATSF spectrum. Table 8.2 shows averages of TRE and P_c for different extremes of τ_m and SMNPR. P_c was estimated in the same manner as in the unmarked case. The TRE data are

Table 8.2 Average TRE and P_c (100 trials) when estimating $(\alpha, \bar{x})$ in the presence of mark noise. $\alpha = 100$, $T = 100$, $\rho_f = 9.93$ (samples/Hz), and SNPR $= \infty$.

σ_m^2	τ_m	P_c	TRE (%)
10	10	0.86/0.16	247/283
1	10	0.79/0.11	51/33
0.1	10	0.86/0.05	4/4
10	1000	0.86/0.11	296/312
1	1000	0.78/0.08	59/32
0.1	1000	0.86/0.04	5/6

shown graphically in Fig. 8.1. They indicate an approximately inverse relationship between the SMNPR ratio and the TRE. This suggests that significant errors will be introduced into the measurement process if the SMNPR is smaller than about 10. The average TRE values for the larger value of correlation length are consistently larger, but the differences are less than two standard deviations of the sample means, so this observation may not be significant.
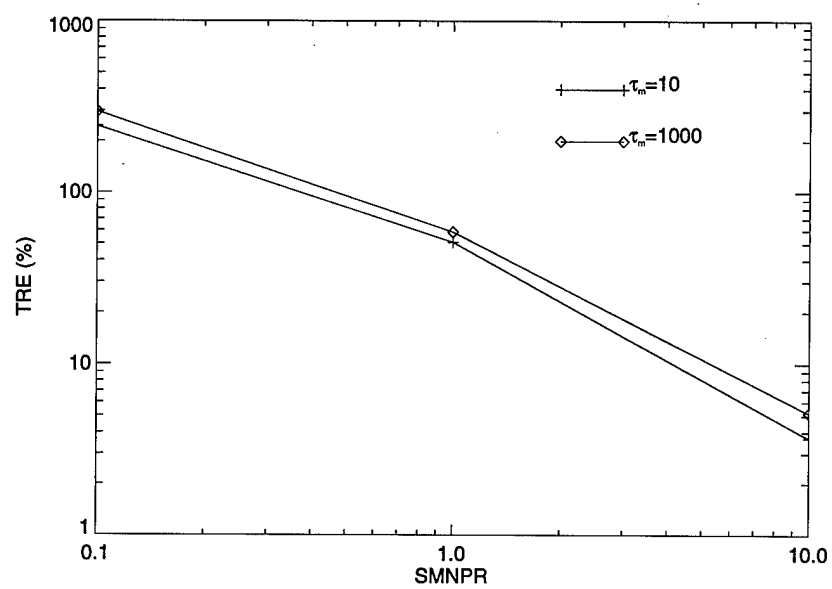
Figure 8.1   TRE as a function of SMNPR when estimating $(\alpha, \bar{x})$ in the presence of mark noise.

9. CONCLUSIONS

This thesis has examined the application of surface regularity models to the problem of measuring surfaces with coherent illumination. We presented a new expression for the PSD of the SRP which describes the scatterer distribution, and developed the mean ATSF power spectrum as an approximate expression for the mean power spectrum of a finite interval of the SRP, which is empirically shown to be valid for all but very short sample intervals and large values of model order, α. Both expressions are valid for both integer and non-integer values of α. The approximation incorporates the windowing effect caused by editing or range gating without the computational burden of performing a convolution. Since the simple periodogram directly estimates the mean power spectrum of windowed data, we take the approach of estimating the model parameters by minimizing the total squared error between the periodogram and the approximation. The merit of this approach is its relative simplicity, since we avoid more elaborate schemes that would require more sophisticated spectral estimation procedures. This is often desirable, since the goal is accurate estimation of the model parameters, rather than accurate estimation of the PSD. The drawback of the approach is that the frequency resolution limitations of the periodogram limit its utility when $T/\bar{x}$ is small.

Use of the approximation and periodogram in this way defines the parameter estimation procedure as an error minimization problem. By restricting ourselves to the use of a wideband periodogram estimate with uniformly spaced frequency samples, we have been able to examine some of the relevant properties of ATSE surfaces. These properties suggest a search strategy to efficiently find the optimal parameter estimates.

The error of the ATSF approximation only hinders parameter estimation when $T/\bar{x}$ and α are mutually small. The TRE of the global minimum of the ATSE surface places a lower limit on the accuracy of a parameter estimation scheme seeking to minimize the ATSE. This TRE is inversely proportional to the square-root of the periodogram SNPR, and is approximately unchanged if the product of T and SNPR is constant. The TRE for the SNPR=∞ case is typically less than 1%, except at very small frequency sampling rates. At a finite SNPR, the TRE decreases slightly as α increases. These observations together suggest that the accuracy of the parameter estimate obtained by minimizing the ATSE is limited primarily by the periodogram SNPR.

P_c is relatively unaffected by the SNPR, but it does depend on α. An estimate of the frequency sampling rate above which P_c is both large and stable is $\rho_f^{80\%} = 0.02\alpha + 4.0$ (samples/Hz). This rate shares a linear dependence on α with various potential measures of the Nyquist rate, but is significantly smaller at large values of α. Since the bandwidths of successive peaks of the PSD decrease with frequency, chirped sampling rates which reduce the sampling rate for higher-order spectral peaks may further reduce sampling rate requirements; this subject is left for future research.

The ability to estimate the model parameters at sparse frequencies in the wide-band measurement case indicates that similar success could be achieved by matching narrow-band measurements directly to the PSD (2.13). In this scenario, the narrow-band, frequency-agile system could measure information about surface properties on scales below that of the system resolution. We leave the analysis of this situation for future research.

Assuming a damped-sinusoidal form for the mark autocorrelation, we present expressions for the PSD of the marked regularity process in the case where the marks are sequentially correlated, and develop closed-form approximations of the mean power spectrum of finite intervals of the marked process in both the sequential and temporally correlated cases. We find that the additional approximation error incurred by

accounting for the marks is not significant, so there is little penalty for using these approximations. Joint estimation of the regularity and mark parameters seems limited to the case where the marks have significant power with respect to the scatterer process, because the mark autocorrelation length is difficult to estimate by minimizing the ATSE surface. Estimation of only the regularity model parameters in the presence of mark noise seems feasible when the mark process is accounted for, but not when it is ignored. The cost of accounting for the marks is a greater computational burden, because the ATSE becomes at least four-dimensional.

BIBLIOGRAPHY

[1] A. A. Sanderson, "Input-output analysis of an IPFM neural model: Effects of spike regularity and record length," *IEEE Trans. Biomed. Eng.*, vol. BME-27, pp. 120–131, March 1980.

[2] L. Landini and L. Verrazzani, "Spectral characterization of tissues microstructure by ultrasounds: A stochastic approach," *IEEE Trans. Ultrason. Ferroelec. Freq. Contr.*, vol. 37, pp. 448–455, September 1990.

[3] K. A. Wear, R. F. Wagner, M. F. Insana, and T. J. Hall, "Application of autoregressive spectral analysis to cepstral estimation of mean scatterer spacing," *IEEE Trans. Ultrason. Ferroelec. Freq. Contr.*, vol. 40, pp. 50–57, January 1993.

[4] N. C. Currie, J. D. Echard, M. J. Gary, A. H. Green, T. L. Lane, and J. M. Trostel, "Millimeter-wave measurements and analysis of snow-covered ground," *IEEE Trans. Geosci. Remote Sensing*, vol. 26, pp. 307–317, May 1988.

[5] J. P. Fitch, *Synthetic Aperture Radar*. New York: Springer-Verlag, 1988.

[6] R. L. Jordan, B. L. Huneycutt, and M. Werner, "The SIR-C/X-SAR synthetic aperture radar system," *IEEE Proc.*, vol. 79, p. 827, June 1991.

[7] F. T. Ulaby, R. K. Moore, and A. K. Fung, *Microwave Remote Sensing: Active and Passive*, vol. 1. Norwood, MA: Artech House, 1981.

[8] F. T. Ulaby, R. K. Moore, and A. K. Fung, *Microwave Remote Sensing: Active and Passive*, vol. 3. Norwood, MA: Artech House, 1986.

[9] F. T. Ulaby, F. Kouyate, A. K. Fung, and A. J. Seiber, "A backscatter model for a randomly perturbed periodic surface," *IEEE Trans. Geosci. Remote Sensing*, vol. GE-20, pp. 518–528, October 1982.

[10] F. T. Ulaby, R. K. Moore, and A. K. Fung, *Microwave Remote Sensing: Active and Passive*, vol. 2. Norwood, MA: Artech House, 1982.

[11] Y.-T. Zhang, C. B. Frank, R. M. Rangayyan, and G. D. Bell, "Mathematical modeling and spectrum analysis of the physiological patello-femoral pulse train produced by slow knee movement," *IEEE Trans. Biomed. Eng.*, vol. 39, pp. 971–79, September 1992.

[12] D. R. Cox and P. A. W. Lewis, *The Statistical Analysis of Series of Events*. New York: Wiley, 1966.

[13] O. A. Z. Leneman, "Random sampling of random processes: Impulse processes," *Inf. Control*, vol. 9, pp. 347–362, 1966.

[14] G. Gestri and P. Piram, "On the autocorrelation of one class of non-stationary random point processes," *Biol. Cybernetics*, vol. 17, pp. 199–205, 1975.

[15] S. L. Marple, Jr., *Digital Spectral Analysis with Applications*. Englewood Cliffs, NJ: Prentice-Hall, 1987.

[16] D. C. Munson and R. L. Visentin, "A signal processing view of strip-mapping synthetic aperture radar," *IEEE Trans. Acoust., Speech, Signal Processing*, vol. 37, pp. 2131–2147, December 1989.

[17] D. R. Cox, *Renewal Theory*. New York: Wiley, 1962.

[18] M. Schwartz, *Discrete Spectral Analysis, Detection and Estimation*. New York: McGraw-Hill, 1975.

[19] A. P. Dempster, N. M. Laird, and D. R. Rubin, "Maximization likelihood from incomplete data via the EM algorithm," *J. Roy. Statist. Soc. Ser.*, vol. 39, pp. 1–38, 1977.

[20] C. F. J. Wu, "On the convergence properties of the EM algorithm," *Ann. Statist.*, vol. 11, no. 1, pp. 95–103, 1983.

[21] L. E. Baum, T. Petrie, G. Soules, and N. Weiss, "A maximization technique occuring in the statistical analysis of probabilistic functions of Markov chains," *Ann. Math. Statist.*, vol. 41, no. 1, pp. 164–171, 1970.

[22] G. Casella and R. L. Berger, *Statistical Inference*. Belmont, CA: Wadsworth and Brooks/Cole, 1990.

[23] IMSL, Inc., *User's Manual: Math Library*. Houston: IMSL, Inc., 1987.

[24] K. E. Atkinson, *An Introduction to Numerical Analysis*. New York: Wiley, 1978.

[25] J. S. Bendat and A. G. Piersol, *Engineering applications of correlation spectral analysis*. New York: Wiley, 1980.

[26] G. R. Cooper and C. D. McGillem, *Probabilistic methods of signal and system analysis*. New York: Holt, Rinehart and Winston, 1971.

[27] A. Papoulis, *Probability, Random Variables and Stochastic Processes*. New York: McGraw-Hill, third ed., 1991.

VITA

VITA

Robert Merrill Cramblitt was born in Baltimore, Md., in 1959. He attended Towson Catholic High School and then majored in electrical enginering at the University of Delaware, where he graduated Summa Cum Laude in June, 1981. He remained at the university to investigate the problem of developing optimal sampling strategies for time-sequential imagery with Prof. Jan P. Allebach, and obtained his Master's degree in 1983. He then worked for the Johns Hopkins University Applied Physics Laboratory, where he developed and analyzed low-light-level imaging systems for ocean measurement programs. He was promoted to Senior Professional Staff in 1989. Later that year he was awarded a United States Air Force Laboratory Graduate Fellowship and took educational leave to work on his doctoral degree in the School of Electrical Engineering at Purdue University. He worked with Asst. Prof. Mark R. Bell on the problem of estimating parameters that describe surfaces characterized by regularity models. He married Catherine D. Axtell in June, 1994, and completed his Ph.D. program in December of the same year. His research interests include modelling and analyzing imaging systems and the scenes they measure, with emphasis on developing new methods to extract information and use it to improve remote sensing and biomedical measurements.

ABSTRACT

Cramblitt, Robert M. Ph.D., Purdue University, December, 1994. Techniques for Sub-resolution Surface Characterization Using Coherent Diversity Measurements. Major Professor: Dr. Mark R. Bell.

This dissertation examines the feasibility of obtaining small-scale surface information from frequency-diverse measurements of surfaces that are stochastically described by a regularity model. This parametric point-process model describes a one-dimensional surface in terms of the mean and variance of the inter-scatterer distances, and can represent scatterer distributions ranging from totally random to nearly periodic. The problem of estimating model parameters from measured spectra is solved by optimizing the total squared-error between closed-form approximations of the mean power spectra of finite-length data intervals and the simple periodogram. The dissertation examines the general performance limitations of such a procedure, determining how approximation error, signal-to-noise ratio and frequency-sampling rate affect the feasibility and accuracy of parameter estimation. We find that parameter estimation is feasible at frequency-sampling rates that are well below that suggested by the PSD. This suggests that it is possible to obtain parameter estimates by comparing sparse narrow-band frequency measurements to the PSD of the point-process, thereby obtaining information about the surface on sub-resolution scales.

The dissertation extends the model to describe marked point processes. We discover that ignoring the marks can cause significant estimation error when estimating the regularity model parameters in the presence of mark noise. Joint estimation of the regularity and mark parameters is feasible only when the variance of the marks is large with respect to their mean. Accounting for the marks can, however, allow the regularity parameters to be accurately estimated in the presence of mark noise.

3205 C Quarry Dr.
Lafayette, IN 47905-5454

December 13, 1994

Prof. Warren D. Peele
Program Director/LGFP
SCEEE Management Office
1101 Massachusetts Avenue
St. Cloud, FL 34769

Dear Professor Peele,

I am pleased to enclose a copy of my Ph.D. thesis, entitled "Techniques for Sub-Resolution Surface Characterization Using Coherent Diversity Measurements." My graduation date will be 18 December, 1994. I wish to thank both the AFOSR and the SCEEE for their support of my graduate program. I will be remaining at Purdue University for the Spring semester in the capacity of Visiting Assistant Professor.

My advisor and I will forward copies of publications arising from this work upon their successful review.

Sincerely,

Robert M. Cramblitt